arXiv:astro-ph/0507427v1 19 Jul 2005

Submitted to ApJ?

Star Formation in NGC 5194 (M51a): The Panchromatic View from GALEX to Spitzer[1]

D. Calzetti[2], R.C. Kennicutt[3], L. Bianchi[4], D.A. Thilker[4], D.A. Dale[5], C.W. Engelbracht[3], C. Leitherer[2], M.J. Meyer[2], M.L. Sosey[2], M. Mutchler[2], M.W. Regan[2], M.D. Thornley[6], L. Armus[7], G.J. Bendo[3], S. Boissier[8], A. Boselli[9], B.T. Draine[10], K.D. Gordon[3], G. Helou[7], D.J. Hollenbach[11], L. Kewley[12], B.F. Madore[8], D.C. Martin[16], E.J. Murphy[13], G.H. Rieke[3], M.J. Rieke[3], H. Roussel[7], K. Sheth[7], J.D. Smith[3], F. Walter[14], B.A. White[3], S. Yi[15], N.Z. Scoville[16], M. Polletta[16], & D. Lindler[17]

ABSTRACT

Far ultraviolet to far infrared images of the nearby galaxy NGC 5194 (M51a), from a combination of space–based (Spitzer, GALEX, and Hubble Space Tele-

[1]Based on observations obtained with the Spitzer Space Telescope and with GALEX.

[2]Space Telescope Science Institute, 3700 San Martin Drive, Baltimore, MD 21218, USA; calzetti@stsci.edu

[3]Steward Observatory, University of Arizona

[4]Department of Physics and Astronomy, The Johns Hopkins University

[5]Dept. of Physics, University of Wyoming

[6]Department of Physics, Bucknell University

[7]Spitzer Science Center, CalTech

[8]Observatories of the Carnegie Institution of Washington

[9]Laboratoire d'Astrophysique de Marseille, Marseille

[10]Princeton University, Observatory

[11]NASA/Ames Research Center

[12]Institute for Astronomy, University of Hawaii

[13]Dept. of Astronomy, Yale University

[14]Max–Planck Institute for Astronomy, Heidelberg

[15]Physics Department, Oxford

[16]CalTech

[17]Sigma Computers Corporation

scope) and ground–based data, are used to investigate local and global star formation, and the impact of dust extinction. The Spitzer data provide unprecedented spatial detail in the infrared, down to sizes ∼500 pc at the distance of NGC 5194. The multiwavelength set is used to trace the relatively young stellar populations, the ionized gas, and the dust absorption and emission in HII–emitting knots, over 3 orders of magnitude in wavelength range. As is common in spirals, dust extinction is high in the center of the galaxy (A_V ∼3.5 mag), but its mean value decreases steadily as a function of galactocentric distance, as derived from both gas emission and stellar continuum properties. In the IR/UV–UV color plane, the NGC 5194 HII knots show the same trend observed for normal star–forming galaxies, having a much larger dispersion (∼1 dex peak–to–peak) than starburst galaxies. We identify the dispersion as due to the UV emission predominantly tracing the evolved, non–ionizing stellar population, up to ages ∼50–100 Myr. While in starbursts the UV light traces the current SFR, in NGC 5194 it traces a combination of current and recent–past SFR. Possibly, mechanical feedback from supernovae is less effective at removing dust and gas from the star formation volume in normal star forming galaxies than in starbursts, because of the typically lower star formation rate (SFR) densities in the former. The application of the starburst opacity curve for recovering the intrinsic UV emission (and deriving SFRs) in local and distant galaxies appears therefore appropriate only for SFR densities $\gtrsim$1 $M_\odot$ yr^{-1} kpc^{-2}. Unlike the UV emission, the monochromatic 24 μm luminosity is an accurate *local* SFR tracer for the HII knots in NGC 5194, with a peak–to–peak dispersion of less than a factor of 3 relative to hydrogen emission line tracers; this suggests that the 24 μ emission carriers are mainly heated by the young, ionizing stars. However, preliminary results show that the ratio of the 24 μm emission to the SFR varies by a factor of a few from galaxy to galaxy; this variation needs to be understood and carefully quantified before the 24 μm luminosity can be used as a SFR tracer for galaxy populations. While also correlated with star formation, the 8 μm emission is not directly proportional to the number of ionizing photons; it is overluminous, by up to a factor ∼2, relative to the galaxy's average in weakly ionized regions and is underluminous, by up to a factor ∼3, in strongly ionized regions. This confirms earlier suggestions that the carriers of the 8 μm emission are heated by more than one mechanism.

Subject headings: galaxies: starburst – galaxies: interactions – galaxies: ISM – ISM: structure

1. Introduction

Over the past decade, discoveries of galaxy populations at earlier and earlier cosmic times has rekindled interest in star formation rate (SFR) indicators, estimated from a variety of monochromatic and non–monochromatic emission measurements across the full spectrum. Of particular interest for cosmological studies are indicators exploiting measurements at restframe ultraviolet (UV), optical, and mid/far–infrared (MIR/FIR) wavelengths; the interest has, however, accompanied a renewed awareness that potential limitations are not fully quantified yet. Presence of even small amounts of dust extinction in the early galaxies hampers significantly SFR measurements from the rest-frame UV emission of the high–redshift galaxies (e.g., the Lyman-break galaxies, Steidel et al (1999); Erb et al. (2003); Giavalisco et al. (2004); Reddy & Steidel (2004)). At the other end of the spectrum, our still limited understanding of the infrared spectral energy distribution of galaxies may decrease the SFR prediction power of the sub–mm emission of the IR-bright SCUBA sources (e.g., Barger, Cowie & Richards 2000; Smail et al. 2000; Chapman et al. 2003, 2004). Even in the local Universe, the widely different angular scales that have characterized until recently UV, optical, and infrared observations of galaxies, ranging from arcsec/subarcsec resolution for UV/optical to multiple arcsecs/arcminutes for FIR (IRAS, ISO), have so far limited our ability to undestand in detail the applicability of each indicator within the realm of physically complex systems (Kennicutt 1998a; Kewley et al. 2002; Rosa–Gonzalez, Terlevich & Terlevich 2002). This in turn has inhibited attempts at cross–correlating calibrations of SFR indicators.

The issue lays in how well tracers at each wavelength can measure the actual SFR. The main problem afflicting UV and optical SFR indicators is dust obscuration. There are two aspects to this problem. One is that regions with moderate amounts of dust will be *dimmed* in a way that depends not only on the amount of dust, but also on the distribution of the emitters relative to the absorbers. This problem is exacerbated by the fact that populations of different ages suffer different amounts of dust extinction (Calzetti, Kinney & Storchi–Bergmann 1994; Charlot & Fall 2000; Zaritsky et al. 2004). Recently it has been shown that quiescently star forming galaxies follow a different dust opacity–reddening relation than starburst galaxies (Buat et al. 2002; Bell 2002; Gordon et al. 2004; Buat et al. 2005; Seibert et al. 2005; Laird et al. 2005). In particular, their IR/UV ratio, a measure of dust opacity, is on average lower than that of starbursts for the same UV color, a measure of dust reddening, and shows a larger spread; differences in the 'b parameter' (the ratio of current–to–lifetime SFR) between star–forming and starburst galaxies has been invoked as an explanation for the observed difference (Kong et al. 2004).

A second problem is the unknown fraction of star formation that is *completely obscured*

by dust at UV and optical wavelengths. The UV and FIR may, indeed, probe different regions/stages of star formation. Heavy obscuration is generally tied to the first temporal phases of star formation, ∼a few Myr; as the stars age, they tend to drift off the parental cloud and diffuse in regions of lower gas/dust density, or to disperse the natal gas/dust cloud (Leisawitz & Hauser 1988). Estimates indicate the fraction of completely obscured star formation to be relatively small in the local Universe, ∼20%–30% (Calzetti et al. 1995a; Heckman 1999; Calzetti 2001), but uncertainties are large and their impact on the calibration of SFR indicators mostly unprobed.

A comprehensive attack to these problems is a core goal of the Spitzer Infrared Nearby Galaxies Survey project (SINGS, Kennicutt et al. 2003). This paper presents the first case study based on the well–known grand–design spiral galaxy NGC 5194 (M51a, Whirpool Galaxy). We use a multi–wavelength dataset of the galaxy by combining UV images from GALEX, ground–based optical images, infrared emission line images from HST/NICMOS (Scoville et al. 2001), and Spitzer 3.5–160 μm images. These data provide a panchromatic view of the star formation in this galaxy, both locally (on the scales of star–formation complexes) and globally. Spitzer and GALEX observations of nearby galaxies (closer than ∼10 Mpc) are uniquely suited for investigating issues of dust obscuration and star formation, thanks to a combination of comparatively high angular resolution (a few arcsec) and the large field-of-views (many arcminutes). We use the multi–wavelength data to investigate the opacity–reddening properties of this quiescently star–forming galaxy on a detailed spatial scale. The UV, MIR and FIR emission are then compared with the optical (nebular lines) emission, both locally and globally, to test the viability of each as a SFR indicator. For instance, the 8 μm emission is a potentially attractive SFR indicator at high-redshifts, as the restframe ∼8 μm PAH bands are redshifted to $\lambda \gtrsim 24$ μm for $z \gtrsim 2$, thus still within the regime probed by, e.g., Spitzer. In addition, unlike tracers that probe directly the stellar light, MIR/FIR SFR tracers are little affected by dust extinction.

There are a number of reasons for why NGC 5194 is an optimal target for this study. At a distance of about 8.2 Mpc (from Tully (1988)'s systemic velocity and H_o=70 km s^{-1} Mpc^{-1}), the typical angular resolution of our mid–infrared data, 5″–13″, corresponds to ∼200–520 pc, or the size of a large star-formation complex. The relatively high level of spatial detail enables us to investigate the nature of the difference in the opacity–reddening properties between starbursts (Meurer, Heckman & Calzetti 1999) and quiescent star–forming galaxies (Kong et al. 2004). The total SFR, ∼3.4 $M_\odot$ yr^{-1}, and the SFR/area, ∼0.015 $M_\odot$ yr^{-1} kpc^{-2}, of this galaxy places it among the 'quiescently' star–forming systems, despite its interaction with the early-type galaxy NGC 5195 (M51b), the latter located about 4′.4 (10.5 kpc) to the North.

NGC 5194 is a nearly–face–on (i$\sim$20^o), grand-design spiral (SAbc), with intense star formation in the center and along the spiral arms. Its OB associations population, the gas they ionize, as well as the diffuse ionized medium, have been extensively investigated at optical and infrared wavelengths (Kennicutt, Edgar & Hodge 1989; Scoville et al. 2001; Thilker et al. 2002; Hoopes & Walterbos 2003). The UV emission shows a strong color gradient as a function of distance from the nucleus, becoming bluer at larger galactocentric distances, based on the GALEX images (Bianchi et al. 2005). This is similar to what was previously found by Hill et al. (1997) from UV−U radial color trends, and a comparison with IRAS images suggest this color gradient to be induced by a gradient in the dust extinction (Boissier et al. 2004). NGC 5194 is a metal–rich galaxy (12+log(O/H)$\sim$8.7–8.9, Bresolin, Garnett & Kennicutt (2004)), with a weak metallicity gradient as a function of distance from the nucleus out to at least 10 kpc radius, or $\sim$75% the B_{25} radius (Zaritsky, Kennicutt & Huchra 1994). When comparing properties of HII knots within the galaxy, the shallow metallicity trend enables us to investigate stellar population ageing effects unencumbered by the metallicity variations that affect galaxy–to–galaxy comparisons.

The present paper is organized as follows: section 2 presents the observations, relevant data reduction considerations, and the main characteristics of the dataset; section 3 is a short overview of the galaxy's morphology at different wavelenghts; section 4 presents the measurements of HII-emitting regions performed on the images; section 5 describes the observed properties of these HII–emitting regions; section 6 presents dust extinction properties; section 7 analyzes the properties of popular star formation rate indicators, while the results are discussed in section 8. A summary is given in section 9.

2. Observations and the Dataset

2.1. Spitzer Images

The Spitzer images of M51 (NGC 5194/NGC 5195) were obtained with both IRAC (3.6, 4.5, 5.8, and 8.0 μm) and MIPS (24, 70, and 160 μm), as part of the SINGS Legacy project. A description of this project and the observing strategy can be found in Kennicutt et al. (2003).

Each of the four IRAC images is a combination of two mosaics, each resulting from a 6×9 grid covering a 18.5′×25′ field. Observations of each mosaic were obtained on 18 and 22 May 2004, allowing a separation of a few days between the two to enable recognition and exclusion of asteroids and detector artifacts. Total exposure times in each filter are 240 s in the center of the field, and 120 s at the edges (outer $\sim$2.5′). The SINGS IRAC pipeline was

used to create the final mosaics, which exploits the sub-pixel dithering to better sample the emission, and resamples each mosaic into 0.76″ pixels (Regan et al. 2004). The measured 8 μm PSF FWHM is 2.1″, and the 1 σ sensitivity limit in the central portion of the 8 μm mosaic is 1.2×10^{-6} Jy arcsec^{-2}.

A 'dust–emission' image at 8 μm is obtained by subtracting the stellar contribution using the recipe of Pahre et al. (2004). The stellar–emission–dominated 3.6 μm and 4.5 μm images are combined assuming colors appropriate for an MIII0 star ([3.6]-[4.5]=-0.15 in Vega mag, Pahre et al. (2004)), and then rescaled under the same assumption to create a stellar–only image at 8 μm ([3.6]-[8.0]=0.0 in Vega mag). A few percent adjustement of the rescaled 'stellar' image is used to optimize the subtraction from the 8 μm image.

Potentially, the 3.6 μm and 4.5 μm images can contain, in addition to photospheric emission from stars, also a component of hot dust emission. The impact of this component relative to the stellar contribution is different in the two images, with flux ratios $[\mathrm{f(dust)/f(star)}]_{3.6}$ $\sim$0.3–0.7 $[\mathrm{f(dust)/f(star)}]_{4.5}$ (depending on the adopted stellar population), for dust with temperature T$\lesssim$1000 K. To test whether a hot dust contribution may affect the derivation of the 8 μm 'dust–emission' image, we have produced a second stellar–continuum–subtracted 8 μm image, using only the rescaled 3.6 μm image as 'stellar continuum'. The two dust images differ from each other by less than 3% across the entire region analyzed, suggesting that hot dust is not significantly impacting the stellar continuum subtraction process.

MIPS observations of the galaxy were obtained on 22 and 23 June 2004. The reduction steps for MIPS mosaics are described in Gordon et al. (2005). The final mosaics have size 27′×60′, fully covering M51 and the surrounding background. At 24 μm, 70 μm, and 160 μm, the PSF FWHM is $\sim$5.7″, $\sim$16″, and $\sim$38″, respectively. The 1 σ detection limits are 1.1×10^{-6} Jy arcsec^{-2}, 8.7×10^{-6} Jy arcsec^{-2}, and 2.6×10^{-5} Jy arcsec^{-2}, respectively, for the 24 μm, 70 μm, and 160 μm images. The three MIPS images are considered 'dust' images for all purposes, as contributions from the photospheric emission of stars is negligible at these wavelenghts.

Consistency between the MIPS and IRAS flux scales has been checked by comparing the MIPS24 with the IRAS25 fluxes and, to a lesser extent, the MIPS70 with the IRAS60 fluxes. We get f(24)$\sim$12.3 Jy for NGC 5194, or about 20% lower than the IRAS25 value of 14.8 Jy (as measured from IRAS HiRes images); for the MIPS70 channel, we get f(70)$\sim$105 Jy, in better agreement with the IRAS60 value of 110.3 Jy, despite the slight offset between the two wavebands. The total far–infrared luminosity of NGC 5194, L(IR)=L(3–1100 μm), as derived from the MIPS fluxes (equations 4 of Dale & Helou (2002)), is Log[L(IR)/(erg s^{-1})]=44.1, about 7% lower than the same quantity obtained from the IRAS fluxes (and using

equation 5 of Dale & Helou (2002)). The nominal MIPS calibration uncertainties, ∼10% at 24 μm and ∼20% in the longer wavelength bands, account for most of the discrepancies between the MIPS and IRAS fluxes and luminosities, with the possible exception of the 24 μm band. However, removal/editing of the companion NGC 5195 is non–trivial in the low resolution IRAS images, and this may account for some of the discrepancy. Indeed, the MIPS24 flux of the whole M51 pair (NGC 5194+NGC 5195), f(24)∼13.5 Jy, is in agrement with the 25 μm flux, ∼13 Jy, obtained by COBE DIRBE (from the DIRBE Point–Source Photometry Browser, http://lambda.gsfc.nasa.gov/product/cobe/browser.cfm).

2.2. GALEX Images

GALEX (Martin et al. 2005) imaging observations are centered at 1529 Å for the far–UV (FUV, 1350–1750 Å) and at 2312 Å for the near–UV (NUV, 1750–2750 Å) bands. Data for M51 were obtained on June 19–20, 2003, as part of the Nearby Galaxies Survey (NGS, described by Bianchi et al. (2004a,b)). The exposure time of 1414 s yields a NUV(FUV) 1-σ sensitivity limit of 1.4×10^{-19} (3.6×10^{-19}) erg s^{-1} cm^{-2} Å^{-1} arcsec^{-2} at the PSF scale (FWHM=4.6″). More details on the GALEX data, and a comparison with previous UIT data, are given by Bianchi et al. (2005). The latest photometric calibrations (IR1 release, November 2004) were applied to the two GALEX images of M51. The measured FWHM of the GALEX PSF is only slightly smaller than the MIPS 24 μm PSF, making the comparison between the two sets of images straightforward.

Distorsions present in the FUV image were corrected by application of non–linear geometric transformations to the image, using the optical images as reference. Residual distorsions amount to $\lesssim$1″.2, negligible for the purpose of this analysis (that employs ∼10 times larger apertures to perform photometry, see section 4).

2.3. HST/NICMOS Images

Observations with HST/NICMOS are available for the central region of NGC 5194 in the Pα emission line (1.8756 μm, F187N narrow–band filter) and the adjacent continuum (F190N narrow–band filter). The image is a 3×3 NIC3 mosaic (GO-7237, P.I.: Scoville) that spans the central 144″, or the inner ∼6 kpc of the galaxy. Details of the observations, data reduction, and mosaicing are given in Scoville et al. (2001).

Because of the proximity in wavelength of the two narrow–band filters, the line–only image is obtained by subtracting the continuum–only image, previously rescaled by the ratio

of the filters' efficiencies, from the line+continuum image. The NIC3 0″.2 pixels undersample the NICMOS PSF, although this is not a concern for the diffuse ionized gas emission of interest here.

The continuum–subtracted Pα image shows a diagonal tilt in the background, which is removed by fitting an inclined linear surface to the image (using the task IMSURFIT in IRAF). The resulting image shows a relatively flat background. The sensitivity is variable, being lower at the seams of the 9 images that form the mosaic. The average 1 σ sensitivity limit of the continuum–subtracted image is 1.8×10^{-16} erg s^{-1} cm^{-2} arcsec^{-2}.

The region of the galaxy imaged in Pα offers a unique opportunity, in conjunction with the Hα image (next section), to directly probe the impact of dust obscuration on the ionized gas, and to measure star formation using an indicator (Pα) weakly affected by dust. An extinction of 1 mag at V produces an extinction of 0.15 magnitudes at Pα, i.e., a small, $\sim$14% change in the line intensity. We adopt an intrinsic ratio Hα/Pα=8.734 (Osterbrock 1989), and differential value k(Hα)−k(Pα)=2.08 for the extinction curve. The central $\sim$6 kpc of NGC 5194 are characterized by observed Hα/Pα ratios that are smaller than the theoretical unreddened ratio, implying attenuations at V in the range A_V $\sim$1–3.4. In what follows, the central region imaged in Pα will be referred to as the Inner Region, while areas external to this will be globally referred to as Outer Region.

2.4. Ground–based Optical Images

Hα–centered narrow–band, B–band, and R–band images were obtained on 28 March 2001, with the Direct Camera at the 2.1–m KPNO telescope, as part of the SINGS ancillary data program (Kennicutt et al. 2003). Exposure times were 1800 s, 720 s, and 360 s for Hα, B, and R, respectively. Standard reduction procedures were applied to the images. Both images are mosaics of 2 frames, displaced along to N–S direction to include both NGC 5194 and NGC 5195. Because of vignetting along one edge of the camera, correction procedures were applied; the photometric integrity along the seam of the mosaic was verified from comparing measurements of stars along the vignetted side of the mosaic with the same stars on the non–vignetted side. Standard stars observations were obtained during the observing run to derive photometric calibrations.

A U–band image of the galaxy obtained on 20 June 2004 with the Steward 90–inch Prime Focus Camera (Williams et al. 2004) is also used in this analysis to construct the stellar population age–sensitive color U−B. The final combined U image is the result of 2 dithered images, with a total exposure time of 1200 s. Photometric calibrations were also

obtained for these observations (Engelbracht et al. 2005a). A comparison of the calibrated U band image of NGC5194 with the analogous image from the Sloan Digital Sky Survey indicates a disagreement between the two calibration scales of 28%, with our image being bluer than the SDSS one. We adopt our own calibration for this work, discussing the impact of the different photometric calibration from SDSS in section 6.1.

The R–band image is rescaled and subtracted from the Hα image, which is then corrected for the contribution of the two [NII](6548,6584 Å) emission lines. We adopt a fixed ratio [NII](6584 Å)/Hα=0.5, although it should be noted that this ratio covers a wide range in NGC 5194, from $\sim$0.3 in individual HII regions up to $\sim$1.9 in the diffuse Hα component (Hoopes & Walterbos 2003). The ratio [NII](6584 Å)/Hα=0.5 is typical of the spatially integrated line emission from a metal–rich galaxy (e.g., compare with M83 in McQuade, Calzetti & kinney (1995)). For a ratio [NII](6548 Å)/[NII](6584 Å)=0.335, the observed line emission is 1.617$\times$Hα. The shallow metallicity trend as a function of galaxy radius (Zaritsky, Kennicutt & Huchra 1994) justifies the use of a single [NII]/Hα ratio for all HII knots in M51.

The absolute photometry of the ground–based Hα image is checked against archival HST/WFPC2 Hα images of M 51. The WFPC2 images cover approximately the same region as the Pα mosaic, i.e., just the inner galaxy region; more details are given in Scoville et al. (2001). The HST images are used to check for three effects: (a) absolute photometry, since our ground–based Hα frames were obtained in marginally photometric conditions; (b) [NII] contamination, since the ground–based images require a large correction, while the HST/WFPC2 Hα filter (F656N) is narrow enough that only a few percent of the total flux is due to [NII] (Scoville et al. 2001); (c) potential oversubtractions in regions with large Hα equivalent widths from using the R–band image (which includes Hα within its bandpass) as underlying continuum, as the HST continnum images exclude Hα.

Points (a) and (b) are not independent, and flux comparisons between 12 common, isolated HII regions, with Hα fluxes between 5.5×10^{-15} and 1.8×10^{-13} and equivalent widths between 25 Å and 500 Å, indicate a mean systematic offset of about 20% between the ground–based and the HST images, the former having lower mean flux than the latter; we correct the ground–based image for this offset. The dispersion around this value is about 20%–25%, and can originate from intrinsic variations of the [NII]/Hα ratio in the HII regions, as observed by Hoopes & Walterbos (2003). We do not correct our individual datapoints for this case–by–case dependent offset, but carry the uncertainties accordingly.

The 1 σ sensitivity limit of our final Hα image is 1.8×10^{-17} erg s^{-1} cm^{-2} arcsec^{-2}. The measured PSF in the optical images is 1.9″, smaller than both the GALEX and Spitzer–MIPS data, and comparable to the PSF of the Spitzer–IRAC data.

3. The Morphology of the Star Formation Tracers

The high–resolution (by infrared standards) maps obtained for this study allow for the first time a comparison of the spatial location of the emission at each wavelength, from the ultraviolet, through the optical, to the infrared for this galaxy. A three–color composite of M51 using three widely used star formation rate indicators (Figure 1, left) shows that the FUV, Hα and 24 μm emission do not always arise from the same regions. In particular, the FUV radiation emerges predominantly along the outer edges of the spiral arms, indicating relatively low dust extinction in these regions, while the FIR dominates the inner edges. The Hα emission appears to preferentially follow the infrared emission, down to a very detailed level, both in knots and in areas of diffuse or filamentary emission. Presence of filamentary dust emission in the inter–arm regions is better appreciated in the higher angular resolution image which combines continuum–subtracted Hα, 3.6 μm continuum emission from the aged, diffuse stellar population, and 8 μm dust emission (Figure 1, right). The complex structure of the dust emission contrasts the relatively smooth stellar emission from the 3.6 μm IRAC image, while, quite expectedly, the Hα emission clusters along the spiral arms as do the brightest knots of dust emission. Along the outermost regions of the spiral arms of NGC 5194, Hα appears relatively unextincted, while dust emission (and extinction) increases steadily towards the center. The 8 μm and 24 μm images also differ in the level of contrast between the luminosities of the arms and inter–arm regions: the contrast is lower, by a factor of 3–4, for the 8 μm dust emission than for the 24 μm emission within the central 15 kpc of NGC 5194.

How can diagnostics, like the FUV and the FIR, derived from light emerging at seemingly different locations effectively provide a good calibration of the star formation?

4. Multiwavelength Photometry of Star Forming Regions

4.1. Aperture Photometry

For the multiwavelength comparisons that are the main goal of this work, all images have been registered to the same coordinate system and pixel scale, using the Hα image as reference. The MIPS 24 μm (MIPS24) images have the lowest resolution, with a PSF FWHM$\sim 6''$[1], and thus will be driving the minimum spatial scale that can be investigated.

[1]Images of observed (IRAC) or simulated (MIPS) PSFs were downloaded from the SSC Instruments' pages at: http://sscspitzer.caltech.edu/obs/ ; FWHMs and aperture corrections (see next section) are calculated from these images.

We choose apertures of 13″ diameter, which correspond to about 520 pc at the distance of the galaxy.

We perform photometry of 166 circular, 13″–diameter, regions in the FUV, NUV, U, B, Hα, dust–only 8 μm, and the 24 μm images, across NGC 5194 (Figures 2 and 3). The regions are selected primarily as being emission peaks in the MIPS24 image, though a second pass is made through the UV images to ensure that bright regions in these are also included. The apertures are selected to be as much as possible non–overlapping, but for a few of them some overlap is unavoidable. In these cases, checks were performed to verify that the flux contained in the overlap region did not exceed 5% of the total flux in either of the two apertures. Of the 166 apertures, 54 are located within the Inner Region probed by the HST Pα image (Figure 3), and for these, the Pα flux is also measured.

In about half of the regions the infrared emission peak and the UV emission peak are visibly displaced relative to each other (Figure 4). The displacement of peaks is of the order of a few arcsec, larger than any displacement expected from mis-registration of the images or from the residual distortions in the GALEX FUV image ($\approx$1″, see section 2.2 above). The large apertures still allow us to encompass both UV and infrared emission, but the measured fluxes are clearly emerging from slightly different regions. Conversely, there is a high degree of coincidence, within the accuracy afforded by the images' resolution, between the infrared, both 8 μm and 24 μm, and Hα emission peaks.

Because of crowding, background annuli are generally difficult to define around each aperture, without including a neighboring region. We thus adopt a different approach for background removal from the measured fluxes. The 166 apertures are divided into 12 'areas' (one of these being the region probed by the HST Pα image), where the local background at each wavelength is fitted and globally removed from each area[2]. Checks performed on the few isolated apertures that can be identified in the images indicate that this process of background removal is robust for the relatively small galactic areas selected (e.g., the Inner Region corresponds to about 20% of D_{25}). The 12 regions used for local background fitting are identified as rectangular areas in Figure 2. The local background has fairly different values from region to region; for instance, it changes by a factor close to 10, from $\sim 10^{-5}$ Jy arcsec^{-2} to $\sim 10^{-4}$ Jy arcsec^{-2} among the 12 regions in the MIPS24 image. As a reference, in the central region background levels at 8 μm and 24 μm represent 32% and 21%, respectively, of the total flux in the region.

[2]The local background is fitted interactively in each image and for each region, using the IRAF routine MSKY written by M. Dickinson (1993). MSKY allows the user to define the interval in the pixels distribution where the mode and the variance are calculated. The interactivity of the procedure produces a robust result even in the absence of source masking.

The definition of background regions is a compromise between selecting small enough areas that a 'local background' can be defined and, at the same time, large enough to include enough pixels that a mode can be robustly derived (see above). Hence, small–level background variations can still be present within each region. To prevent such local variations from significantly affecting our analysis, we adopt a strict definition of 'detection': detections are defined as background–subtracted fluxes that are at least 100% of the local background. Below this level, we define them as 'upper limits'. Within this definition, out of 166 apertures, 33 contain upper limits in one or more bands; 29 of them are in the FUV image. This leaves us with 133 apertures with reliable measurements at all wavelengths. In the Inner Region, of the 54 regions, 43 have measurements in all six bands; for 7 regions Pα is below our detection threshold, and for 4 other regions the FUV is also an upper limit. One of the 133 regions coincides with the Seyfert 2 nucleus (Ford et al. 1985; Goad & Gallagher 1985; Terashima & Wilson 2001; Sturm et al. 2002), which is excluded from our analysis. The UV, optical, and near–IR photometry is corrected for the small foreground extinction from our own Galaxy, E(B−V)=0.037 (from the NASA Extragalactic Database). Table 1 lists of the positions and luminosities of the 132 HII knots defined as 'detections'.

For the U and B bands a stricter approach is adopted for background removal, because of the proportionally larger contribution and inhomogeneity of the underlying galaxy at these wavelengths. In this case, background removal is checked for each aperture, and in case of undersubtraction with the default background regions, smaller, more appropriate background regions are applied as needed.

The uncertainties assigned to the photometric values are a quadratic combination of three contributions: variance of the local background, photometric calibration uncertainties, and variations from potential mis-registration of the multiwavelength images. The variance on the local background is derived from the original–pixel–size images, after projecting each rectangular region on the original images. The effect of potential misregistrations are evaluated by shifting the images by $1''.2$ (the magnitude of the residual distorsions in the GALEX images, section 2.2) relative to each other. Because of the large apertures employed for the photometry, this contribution is either small (a few % of the total uncertainty) or negligible in all cases. An additional contribution to the uncertainties assigned to the wavelength–integrated infrared luminosities is discussed in section 4.3.

4.2. Additional Sources of Uncertainty

The star forming regions that are being studied here can be considered, for all purposes, point sources at the MIPS24 resolution; the aperture corrections are fairly substantial despite

the relatively large apertures (factor 1.67). Aperture corrections are smaller at shorter wavelengths: about 6% and 10% for point sources in the the FUV and NUV GALEX images[3], respectively, and negligible for the ground-based, HST, and IRAC images.

The large MIPS24 PSF can also lead to contamination of the aperture photometry by nearby sources. The photometry in an aperture centered 13″ *away* from a source will include on average 4% of the flux from the contaminating source. Photometry of the target source will be affected in proportion to the flux ratio between the two sources, which can be a significant fraction of the target's flux if the contaminating source is significantly brighter than the target. There are about a dozen apertures in our sample of 132 that contain sources at least twice as faint as the adjacent one, and for which the impact from the neighboring source on the 24 μm flux is 8% or larger. Tests run using samples with or without data from these apertures have produced results that are nearly identical for the trends described in the next sections. This suggests that the influence of those 'affected' apertures is negligible on the general trends. Use of the PSF–fitting method to improve photometry of sources in crowded regions for our lower resolution images is being investigated for possible application to future multi–wavelength analyses of the SINGS galaxies.

Our analysis is based on the assumption that in each single region, the emission at any wavelength is due to the stellar population and dust located in that region. Effects of radiation transfer could in principle be important for the IR measurements, as dust in a region could be heated by UV photons produced outside that region. However: (1) in general, local IR peaks have a one–to–one correspondence to local Hα peaks in our images, across the entire galaxy's disk and center; although heating from out–of–region UV photons cannot be excluded, the observed correspondence suggests that most of the heating in those peaks is produced locally. (2) The subtraction of 'local' backgrounds removes IR flux contributions from the heating by the diffuse stellar population. We thus conclude that for our purposes we can assume the multi–wavelength emission in each aperture to be due mainly to local stellar populations and locally–heated dust.

4.3. Derivation of the Infrared Luminosities

The 13″ diameter apertures, although already large by 'HII-regions-size' standards, are too small to contain a significant fraction of the 70 μm (MIPS70) or 160 μm (MIPS160) PSFs. Therefore, these images cannot be used directly to measure the fluxes of our HII knots at

[3]Aperture corrections for the GALEX photometry were measured from point sources contained in the GALEX images of NGC5194.

the longer wavelengths, raising the problem of estimating total far–infrared luminosities. Conversely, choosing apertures appropriate for photometry in the MIPS70 and MIPS160 images, i.e, $>50''$, would hamper any attempt to investigate the properties of the young stellar populations, the gas they ionize, and the dust they heat. Such apertures correspond to physical sizes 2 kpc or larger at the distance of M51, thus probing significant fractions of the galaxy's integrated population.

We thus determine total infrared luminosities for our HII knots, L(IR)=L(3–1100μm), by exploiting the correlation between the 8 μm–to–24 μm flux ratio and the 24 μm–to–total luminosity ratio (Dale & Helou 2002). We derive the best fit relation for our HII knots as follows. Photometry in 21 $70''$ diameter apertures is performed on the 8 μm dust–only image and on the 3 MIPS images; the 21 regions are selected to target peaks of 70 μm emission in the center of the galaxy and along the spiral arms. The diameter of the regions, corresponding to $\sim$2.8 kpc, are selected to encompass 65% of the light from the 160 μm PSF; the same aperture contains 100%, 94%, and 88% of the light from the PSFs at 8 μm, 24 μm, and 70 μm, respectively. Local background values are subtracted from each region to minimize contamination from dust heated by the the diffuse stellar population(s). Six different local background regions are selected to 'hug' as close as possible small groups of apertures, using an approach similar to the one described in section 4 above. The shape of such background regions is rectangular, with the longer side aligned as much as possible along the direction of the spiral arm containing the photometric apertures. L(IR) for these datapoints is integrated from the MIPS band measurements using equation (4) of Dale & Helou (2002); this relation between the MIPS bands and the total infrared emission is still applicable to our case, as the range of colors of the 21 regions, $-0.5 \lesssim Log[L(8)/L(24)] \lesssim 0.1$ and $0.2 \lesssim Log[L(70)/L(160)] \lesssim 0.7$, is within the range of spectral energy distributions parametrized by those authors.

The resulting plot Log[L(24)/L(IR)] versus Log[$L_\nu(8)/L_\nu(24)$] (where L(24)=$\nu L_\nu(24\ \mu\mathrm{m})$[4]) for the 21 regions is shown in Figure 5, together with the best fit line through the data points; the model of Dale & Helou (2002), appropriate for whole galaxies, is also shown for comparison. The datapoints of Figure 5 are systematically higher than the whole–galaxies predictions of Dale et al., as can be expected if the 24 μm luminosity is proportionally a larger fraction of the total infrared luminosity in the HII knots than in whole galaxies, and the IR spectral energy distributions are typical of hotter dust. Since we have subtracted the diffuse disk emission from the aperture measurements, we expect the longer wavelength

[4]From now on, the convention L(band)=νL_ν(band) is adopted for broad–band flux measurements, where the band can be any of the GALEX, optical, IRAC, or MIPS bands. These 'monochromatic' luminosities are in units of erg s^{-1}.

('cirrus') emisssion to be depressed relative to the case of entire galaxies emission, as the cirrus emission can be heated by the diffuse stellar field (Helou 1986; Boulanger et al. 1988). Indeed, the location of the emission from the whole galaxy in Figure 5 is along the 'lower envelope' of the locus defined by the HII knots, in line with the above reasoning. The full discussion of this aspect of the IR spectral energy distribution of NGC 5194 and other local star–forming galaxies will be undertaken elsewhere (Dale et al. 2005).

The best fit straight line through the datapoints of Figure 5 provides the following relation:

$$Log[L(IR)] = Log[L(24)] + 0.908 + 0.793 Log[L_\nu(8)/L_\nu(24)], \quad (1)$$

which we adopt in the following as our baseline relation for deriving total infrared luminosities for the 13″–diameter apertures. The scatter around the best fit line is ±40%, and we factor this scatter in the uncertainty budget of L(IR). According to this relation, the 24 μm luminosity represents 7%–21% of the total infrared luminosity. The datapoints in Figure 5 cover a somewhat smaller 8/24 μm ratio range than that covered by the data in the smaller apertures ($-0.4 \lesssim \mathrm{Log}[L_\nu(8)/L_\nu(24)] \lesssim 0.2$); we assume that our best fit line can be extrapolated 0.2 dex towards smaller 8/24 μm ratios, to include all the smaller aperture datapoints.

Our selection of local background values for the 70″–diameter apertures should still be considered a 'best attempt', as the typical background region has sizes ∼4×8 kpc^2, thus encompassing a significant fraction of the galaxy's population. We, thus, cannot exclude that the data in Figure 5 and equation (1), and in particular the 160 μm measurements, are partially contaminated by cirrus emission extraneous to the HII blob infrared emission. In what follows, we assume that this contamination represents a small fraction of the total infrared emission.

5. Observed Properties of the Star–Forming Regions

The selected 166 star–forming regions cover a factor ∼300 in 24 μm luminosity (L∼10^{39}–$10^{41.5}$ erg s^{-1}), and ∼100 in FUV luminosity (Figure 6). The knots in the Inner Region tend to be overluminous at 24 μm for constant FUV luminosity relative to the knots in the Outer Region, and to have on average redder UV colors (section 6); not surprisingly, this reflects higher dust extinction in the Inner Region relative to the Outer. There is no significant difference in the distribution of the $L_\nu(8)/L_\nu(24)$ flux ratios or in the mean Hα luminosity between the Inner and Outer Regions.

None of the selected knots, not even the UV–selected ones, is consistent with the UV

colors expected for a ionizing, dust–free stellar population (younger than ∼10–12 Myr, Figure 7). Nearly all of the knots contain at least a small amount of infrared emission implying presence of dust. Stellar population ageing is also a possibility, especially for those cases where there is a displacement between infrared and UV peaks within the photometric apertures.

For both the Inner and Outer Regions, there is a clear trend for more luminous Hα regions to have hotter FIR spectral energy distributions (lower 8/24 μm flux ratios, Figure 8). This correlation persists when extinction–corrected Hα luminosities are used (see section 6.1). As will be seen later, the anticorrelation between the IR colors and the Hα luminosity is due to the 8 μm luminosity becoming underluminous for increasing Hα luminosity.

6. Dust Extinction Properties

6.1. The Impact of Dust and Age on the UV

The ratio of the infrared to far–UV luminosities is a measure of the total dust opacity experienced by the UV stellar continuum in a region, and this quantity has been shown to correlate tightly with the UV colors of starburst galaxies (Meurer, Heckman & Calzetti 1999). In NGC 5194, the total UV opacity L(IR)/L(FUV) is also related to the UV colors for the 132 HII knots, but with a significantly larger scatter than in the case of starbursts (Figure 9, left). In particular, at fixed UV color, the IR/FUV ratio of the HII knots spans about one order of magnitude larger range than the IR/FUV ratio of starburst galaxies. In addition, the locus identified by the starburst galaxies in the IR/FUV–UV color plane represents the *upper IR/FUV envelope* to the HII knots; with few exceptions, the HII knots in NGC 5194 have IR/FUV ratios that are lower than those of starbursts, at fixed UV color (see, also Bell et al. 2002). However, even among the HII knots there are no regions that can be at the same time red and IR–faint. Indeed, despite the large scatter, there is still a good correlation between the HII knot datapoints; a non–parametric rank test indicates that the correlation is significant at the 7.2 σ level. Such level of correlation implies that the UV reddening still follows the total UV opacity, albeit with a different slope and scatter than starbursts.

To remove any doubt on the location of the HII knots' datapoints relative to those of the starburst galaxies, we investigate whether there may be an impact on such location from the way L(IR) is calculated for the HII knots in NGC 5194, i.e., using the approximation of equation (1). The right–hand side plot of Figure 9 shows the same IR/FUV versus UV color plot, where L(IR) is replaced by the directly measured L(24). Data for 29 starburst

galaxies from the sample of Calzetti et al. (1994) are reported on the same plot, using the IRAS 25 μm measurements in lieu of MIPS24. Again, the relation for the starburst galaxies and the NGC 5194 knots are offset, with the starbursts defining the upper envelope of the correlation.

In Figures 9–12 the data are compared with stellar populations models convolved with dust extinction models. Stellar population models are from Starburst99 (Leitherer et al. 1999), either instantaneous bursts or constant star formation, with solar metallicity (to roughly match the metallicity of NGC 5194) and Salpeter stellar Initial Mass Function in the range 1–100 $M_{\odot}$. Dust models employ both the Milky Way (MW, with R_V=3.1, Cardelli, Clayton & Mathis 1989) and Small Magellanic Cloud (SMC, Bouchet et al. 1985) extinction curves. The dust geometries investigated include foreground, non–scattering dust screens, homogeneous mixtures of dust, gas, and stars, and the starbursts' dust distribution (Calzetti, Kinney & Storchi–Bergmann 1994; Meurer, Heckman & Calzetti 1999; Calzetti et al. 2000). The latter is equivalent to a clumpy shell surrounding the starburst volume, where the ionized gas suffers about twice the attenuation of the stellar continuum (Calzetti 2001). Colors and luminosities are obtained by convolving the stellar plus dust models with the appropriate filter's passband; the infrared luminosity is calculated assuming that the scattering component of the extinction averages out, and all extincted stellar light is re-emitted by dust in the infrared.

The UV reddening of the starbursts is originally expressed as their spectral slope β_{26}, defined as the UV slope in the 0.13–0.26 μm range ($f(\lambda) \propto \lambda^{\beta}$, Calzetti, Kinney & Storchi–Bergmann (1994)); β_{26} has been converted to equivalent GALEX UV colors using the formula:

$$Log[L_{\lambda}(FUV)/L_{\lambda}(NUV)] = -0.1688\beta_{26} - 0.0177, \quad (2)$$

where L_{λ}(FUV) and L_{λ}(NUV) are luminosity densities expressed in units of erg s^{-1} $Å^{-1}$; negative values of β_{26} correspond to blue UV colors. The conversion between β_{26} and the GALEX UV colors is not unique, and depends on the physical parameter driving the color variation. Equation (2) is valid for variations in color due to variations in dust reddening, as is the case for the starburst sample of Calzetti, Kinney & Storchi–Bergmann (1994). Were the variation driven by the ageing of a dust–free stellar population, the conversion formula would be:

$$Log[L_{\lambda}(FUV)/L_{\lambda}(NUV)] = -0.1435\beta_{26} + 0.04102, \quad (3)$$

where β_{26} is measured in the age range 2–300 Myr.

To assess the origin of the large scatter for the IR/FUV–UV colors of the HII knots in NGC 5194 and their variance relative to starburst galaxies, we investigate two possible origins: (1) presence of ageing, albeit UV–emitting, stellar populations; (2) differences in the

dust geometries of the starbursts and the HII knots.

6.1.1. Stellar Population Ageing

Although each of the HII knots is a region ∼520 pc in size, and may encompass more than one stellar cluster (single–age population), we still attempt to model the *dominant source of UV emission* in each aperture as an instantaneous burst population. Figure 10 shows the effect of including stellar population ageing in the IR/FUV–UV colors plot. The model lines in Figure 10 are obtained by combining instantaneous burst populations (Starburst99, Leitherer et al. (1999)) with the starburst opacity curve (Calzetti, Kinney & Storchi–Bergmann 1994; Calzetti 2001). About 92% of the HII–emitting knots in NGC 5194 have their IR/FUV ratios and UV colors well described by instantaneous burst populations in the age range 2–300 Myr, provided their dust attenuation and reddening characteristics are similar to those of the starburst galaxies. Within this model, the maximum opacity experienced by the HII knots corresponds to $A_V \lesssim 2.8$ mag[5].

Incidentally, the UV–selected knots have generally low IR/FUV colors (low dust opacity) and, at the same time, red UV colors, suggesting that even in this specific case, the UV–bright knots are consistent with ageing stellar populations.

For the Inner Region, the Hα/Pα line ratio offers an independent measure of dust reddening to further investigate the properties of the knots. The UV colors of knots in this region show a trend to be redder for higher extinction A_V (Figure 11, left), as expected if dust is present. The points show a fairly large spread at fixed A_V. For a starburst opacity curve, this spread cannot be reproduced by dust reddening alone; rather, for each value of A_V, a spread in age, from 2 to ∼300 Myr is present. In this plot, the HII knots in the NGC 5194 Inner Region do not appear qualitatively different from the starburst galaxies, in the sense that the age spread at fixed A_V appears similar in both samples. This 'similarity' is likely due to the small dynamical range of the UV colors, and is broken once a longer wavelength baseline is considered. The FUV/Pα luminosity ratio spans indeed a narrower range, at fixed dust opacity, for the starburst galaxies than for the NGC 5194 Inner Region knots (Figure 11, right). We then use the U−B color to better constrain the age spread of

[5]In the context of this work, A_V will be used only to refer to the attenuation of the ionized gas. If the dust geometry in the region follows the starburst attenuation curve, the attenuation at V appropriate for the *stellar continuum* is A_V^{star}=0.44 A_V^{gas}, where in our convention $A_V^{gas} \equiv A_V$. This convention will be maintained also in the case of evolved stellar populations, i.e. populations older than ≈10 Myr, where no ionized gas is expected to be present.

the latter.

The Log[L_λ(U)/L_λ(B)] color is a sensitive age indicator, because it straddles the 4000 Å break of stellar populations. This color is not as dust–insensitive as the D(4000) age indicator, extensively used in SDSS studies (Kauffmann et al. 2003), but it is far less sensitive than any of the colors we have used so far. In particular, Log[L_λ(U)/L_λ(B)] has more than twice the dynamical range in age, and less than half the sensitivity to dust extinction than the GALEX UV colors (for a non–MW dust, Figure 12, left). The extinction–corrected Log[L_λ(U)/L_λ(B)] colors of the Inner Region's knots indicate an age range 3–100 Myr (Figure 12). This age range would change to ∼5–200 Myr, if the SDSS calibration for the U–band image of NGC 5194 were adopted (section 2.4). Changing assumptions on the dust extinction curve or geometry will only minimally affect the corrected U−B colors, implying that the knots span a considerable age range, from a few Myr to 100–200 Myr. The observed U−B colors of the apertures in the Outer Region are consistent with those of the Inner Region, showing a similar spread in age. Thus, the different behavior of starburst galaxies and NGC 5194 HII knots in the IR/FUV–UV color plane is driven by ageing of the stellar populations in the knots.

The question arising at this point is: how are the UV emission and the ionized gas emission related to each other? Any knot with UV or U−B color ages older than ∼10–12 Myr should not be producing detectable ionized gas emission (Leitherer et al. 1999). This conundrum can be reconciled if each aperture, covering ∼520 pc in the galaxy, contains multiple stellar populations; within each region, these populations are likely to cover a range of ages, masses, and dust extinctions. The stellar populations which dominate the ionized gas emission are not always the same ones that dominate the UV (and longer wavelengths) stellar continuum emission. As an example, Figures 10–12 show the colors and flux ratios expected for a model obtained by combining two stellar populations: a 5 Myr old burst and a 300 Myr old burst, reddened by the starburst opacity curve. In this specific example, the 5 Myr old cluster has a mass 300 times lower than the 300 Myr old cluster (section 8.2), and an excess extinction ΔA_V=+0.25 mag relative to the older cluster (section 8.1.1), except for A_V=0, where both populations are extinction–free. The tracks and colors identified by this very simple 2–populations model account for the intermediate–to–old range of ages for the datapoints in the Figures 10–12. Varying the difference in age, mass, and dust extinction, and the number of separate populations, will likely account for the full observed range of colors of the HII knots. The findings of section 4, where it was noted that in about half of the knots the UV and line emission peaks are spatially displaced relative to each other further support the case for the presence of multiple stellar populations.

6.1.2. Variations in Dust Geometry

Although age differences in the stellar populations dominating the knots' UV emission appear to be likely responsible for the differences between starburst galaxies and NGC 5194 HII knots in Figure 9, we still need to investigate whether differences in dust geometry between starbursts and the quiescently star–forming galaxy could also contribute to the effect.

The Galactic (MW) extinction curve fails to reproduce either the UV colors or the IR/FUV ratios of the HII knots (Figures 9 and 11), for both foreground dust or mixed dust–stars–gas geometries. We take here the foreground and mixed distributions as two extremes of a continuum of possible dust geometries. A more extreme geometry than the mixed one is the Cloudy model (Witt & Gordon 2000), where a dust–free stellar population is located in front of a mixed dust–stars distribution. However, the purely mixed geometry is sufficient for our current purposes. The clear answer we can gain on the MW extinction curve is due to the characteristics of the GALEX filters. The GALEX NUV filter is centered on the 2200 Å bump of the MW extinction curve, and the differential reddening relative to the FUV filter is small. Hence, UV colors tend to be insensitive to effects of dust extinction for a MW curve, irrespective of geometry. The fact that, however, the HII knots show a clear trend to have redder colors for higher opacity values is indicative that the extinction curve in NGC 5194 has a weaker 2200 Å feature than the MW dust.

A Small Magellanic Cloud–like extinction curve appears to be more adequate at explaining the datapoints in the UV colors–A_V plane (Figure 11). The HII knots data are bracketed between the SMC mixed dust and SMC foreground dust geometries (in particular the foreground geometry with A_V^{star}=0.5 A_V^{gas}, indicated as SMC(0.5*A_V) in Figure 11). However, the same geometries are inadequate to account for the observed range of IR/FUV (Figure 9). In particular, a considerable number of HII knots has systematically too low a IR/FUV ratio at any given UV color even for the foreground SMC dust, and even after taking into account photometric undertainties.

Thus, although variations in the dust geometry between starbursts and the HII knots cannot be completely excluded (Bell et al. 2002), they are unlikely to be the main drivers of the observed scatter below the starburst curve mean trend (Figure 9). Age variations between the UV–emitting populations are more likely to be the second parameter to the relation (Figures 10 and 11).

6.1.3. Dust Opacity and Star Formation

The total IR+FUV luminosity and the dust opacity, expressed as IR/FUV (Figure 13), are correlated for the HII knots in the Inner and Outer Regions, with a 5.1 σ significance, using a non–parametric rank test. For actively star–forming galaxies, the sum of the infrared and far–UV luminosities is for all purposes the total UV light from the region (both direct and dust–absorbed, Wang & Heckman 1996; Heckman et al. 1998), which is proportional to the star formation rate (Kennicutt 1998a). The existence of a such a correlation for the NGC 5194 HII knots testifies to the dominant role of dust extinction over population ageing trends, the latter being a secondary parameter. Incidentally, the best fit line determined by Heckman et al. (1998) for starburst galaxies is also a reasonable fit to the knots, modulo a vertical rescaling to account for the intrinsic faintness of the HII knots relative to the starbursts (Figure 13). The peak–to–peak spread, ∼1 dex, around the mean behavior is, as seen in the previous section, the effect of the multiple–age stellar populations contributing to the emission in each aperture, together with possible contribution from spatially variable dust geometries. Interestingly, this spread is still smaller than the one observed for starburst galaxies (Heckman et al. 1998), owing to the more homogeneous nature of our HII knots.

A tantalizing characteristic of Figure 13 is that the majority of the UV–selected datapoints is located to the left of the best fit correlation, and offset from the main locus of the other data. This is expected if the UV emission in those regions is from evolved stellar populations (Figure 10), unrelated to the current star formation. In such a case, the IR/FUV ratio decreases and the IR+UV luminosity increases because of the addition of unrelated UV emission, in a way that tends to push the datapoints away from the main locus of all the other data.

6.2. Radial Trends of Dust and Age

The *median* A_V decreases as a function of the distance from the nucleus, while the *median* UV color becomes bluer (Figure 14). The trend for A_V is reported for both our baseline 13″–diameter apertures and the 4″–diameter apertures. The scatter around the median A_V also increases for larger nuclear distances. Indeed, regions as reddened as the very central ones are present at 3 kpc as well, but for increasing nuclear distance the number of regions with very low extinction increases as well. In particular, while the area about 500 pc from the nucleus is characterized by A_V values in the range 2.8–3.6 mag, the region ∼3 kpc away has A_V values in the range 1–3.4 mag. The knots closer to the center also display on average lower MIR color ratio L(8)/L(24) (hotter IR SEDs) than the more distant knots, but as in the case of A_V the scatter also increases as a function of distance. The UV colors

follow the general trend of A_V, but their scatter around the median remains roughly constant with galactocentric distance, contrary to the increase of scatter in both A_V and L(8)/L(24).

The tighter scatter displayed by the UV colors as a function of galactocentric distance is due to the combined effects of decreasing dust attenuation and decreasing mean age of the HII knots (Figure 15, left). The extinction–corrected $L_\lambda(U)/L_\lambda(B)$ color shows indeed that mean ages decrease as a function of distance from the nucleus, from <100 Myr close to the center down to <20 Myr at a distance of ∼3 kpc from the center. While the knots closer to the nucleus are older than the more distant knots, they are still more luminous in Pα (Figure 15 right), suggesting that: (1) multiple–age populations co-exist within each knot; (2) the inner knots are more massive (at fixed age) than the more distant knots.

The distribution of A_V values has median value ∼2.6 mag for the 13″ apertures and ∼2.8 mag for the 4″ apertures (Figure 16). For comparison, Scoville et al. (2001) measure a median value A_V ∼2.9, in 1″ apertures, with extinction values as high as A_V ∼6 mag, after rescaling for the slightly different intrinsic value of Hα/Pα used in this paper. The trend for larger apertures to yield smaller values of A_V and narrower distributions is a well known effect, due to the higher level of blending between HII regions of different A_V values and increasing amounts of diffuse gas included in the larger apertures. An analysis of the Pα image shows that the level of blending is from a few to many tens of HII regions in each aperture. Our observed range of A_V is ∼1–3.6 mag for the 13″ apertures, consistent with the range measured by van der Hulst et al. (1988) using the Hα/radio ratio in apertures of comparable size. In NGC 5194, the diffuse gas suffers from a lower mean extinction than the HII regions, A_V ≈2 mag, as shown in Scoville et al. (2001).

7. The Infrared Emission as a Star Formation Rate Indicator

The high angular resolution of the Spitzer images enables a detailed comparison of the infrared emission with the ionized gas emission for the HII knots. Both types of emission are used as SFR tracers in star–forming/starburst galaxies: the infrared emission measures the dust-reprocessed stellar continuum emission from massive stars, while the ionized gas emission is proportional to the number of ionizing photons (e.g., Kennicutt 1998a; Kewley et al. 2002). In principle, for the infrared emission to be an accurate tracer of SFR, all of the UV light from massive stars needs to be absorbed by dust (Kennicutt 1998a). The large dust attenuation (A_V >1 mag) and IR/FUV ratio values of the Inner Region indicate that the approximation L(IR)∼L(FUV) is legitimate in the center of NGC 5194. In this region, the Pα emission line, which is only modestly impacted by dust obscuration, is used to measure the number of ionizing photons.

The infrared luminosity of the Inner Region's HII knots correlates tightly with the extinction–corrected Pα luminosity (Figure 17), with a linear best fit:

$$Log[L(IR)] = (0.90 \pm 0.07) Log[L(P\alpha)] + (7.4 \pm 2.8). \quad (4)$$

This relation is about 1.5 σ discrepant from a slope of unity; the error bars on the individual datapoints are large (Figure 17) and mainly driven by the uncertainties in equation (1). The deviation of the slope of equation (4) from unity is small, and it is in the direction expected if the infrared emission from fainter HII knots is proportionally more contaminated by contributions from evolved populations present in the aperture than brighter HII knots are. These evolved populations are unrelated to the current SFR probed by the ionizing photons. This effect is likely impacting also the integrated infrared emission of the Inner Region, which is larger than what predicted by either the best fit line or the unity–slope line (Figure 17).

The sum of the infrared and FUV light has been used as a SFR tracer for star–forming/starburst galaxies, as it measures all of the available ultraviolet light from massive stars, both directly observed and dust-reprocessed (Wang & Heckman 1996; Heckman et al. 1998). This appears not to be the case in the Inner Region of NGC 5194, where the FUV emission is probing a range of stellar populations, including ageing, non–ionizing ones (section 6.1.1). For the HII knots, although L(IR+FUV) is correlated with L(Pα), the best fit line is:

$$Log[L(IR + FUV)] = (0.81 \pm 0.07) Log[L(P\alpha)] + (10.1 \pm 2.8), \quad (5)$$

with a slope much shallower than unity ($\sim$3 σ) than the one of equation (4). The contribution of the UV light mainly affects the data at the faint IR end, hence the shallow slope. L(IR+FUV) is probing star formation on a longer timescale ($\approx$100 Myr) than L(Pα) ($\approx$10 Myr).

The Pα and 24 μm luminosities of the HII knots show a tight correlation (Figure 18), and a linear fit through the data of the 42 regions gives:

$$Log[L(24)] = (1.03 \pm 0.04) Log[L(P\alpha)] + (0.9 \pm 1.3), \quad (6)$$

after removing the faintest 24 μm datapoint. This fit is not significantly discrepant from a slope of unity. In terms of SFRs, equation (4) implies that the 24 μm emission is as good an indicator as the Pα, with a typical dispersion around the median of $\sim$0.2 dex. The extrapolation of equation (4), which is derived for the HII knots, to the integrated Pα luminosity of the Inner Region reproduces the 24 μm luminosity of this region (Figure 18), as expected if the two luminosities closely trace each other. Equation (6) quantifies the close spatial correlation between 24 μm emission and star forming regions found by Helou et al. (2004) in the disk of NGC 300.

Although equation (6) provides so far the best linear correlation between infrared luminosities and L(Pα), some care should be taken in concluding that the 24 μm luminosity provides a reliable SFR tracer for galaxies in general. The ratio L(24)/SFR is constant within the relatively uniform environment of the central region of NGC 5194, and provides a locally accurate SFR tracer. However, it also changes from galaxy to galaxy. In particular, the locus in L(24)/SFR ratio identified by UV–selected starbursts and by ULIGs is systematically higher than the ratio from the NGC 5194 HII knots (Figure 19). As will be discussed later, local conditions can determine the strenght of the 24 μm luminosity relative to SFR and possibly account for the observed variability from galaxy to galaxy (Dale et al. 2001).

At mid–infrared wavelengths, the 8 μm dust luminosity also correlates tightly with the Pα luminosity, implying that regions brighter at one wavelength are also brighter at the other, but the slope is significantly discrepant from unity (Figure 20, left). A linear fit gives:

$$Log[L(8)] = (0.79 \pm 0.02) Log[L(P\alpha)] + (10.6 \pm 0.7), \quad (7)$$

after removing the faintest 8 μm point. The fitted slope is about 10 σ away from unity. The extrapolation of the fit to the Pα value of the entire Inner Region would underestimate the 8 μm luminosity for this region by a factor 3.2.

The fairly large, 13″, apertures used to derive equation (7) include, potentially, a significant fraction of diffuse emission in the 8 μm photometry. This may artificially increase the 8 μm emission of fainter regions, thus flattening the overall trend. However, the same fit repeated for photometry in the 78 smaller, 4″–diameter, apertures provides a fit with slope (0.80 ± 0.02), which is within the uncertainties, identical to the slope of the larger apertures fit. The datapoints for the two sets of apertures are in remarkable agreement (Figure 20), despite the large aperture correction, a factor 1.75, required by the 8 μm measurements in the smaller apertures.

For the small aperture photometry, one concern is of a potential artificial increase of the 8 μm flux of those faint regions adjacent to bright regions, because of the flux contribution from the PSF wings of the bright region (section 4.1). In particular, photometry in an aperture centered 4″ away from a bright source would include on average 5.5% of the bright neighbor's flux, thus impacting measurements of any faint source in the aperture. We have repeated the fit on the 4″–diameter datapoints after removing all sources located less than 2 diameters away from sources at least twice as bright. The remaining datapoints (72) give a best fit slope (0.83 ± 0.03), very similar to the slope of the entire sample of 78 sources.

The 8 μm luminosity still shows a very significant deviation from a slope of unity in the combined Inner+Outer regions, when plotted as a function of the 24 μm luminosity, used as

a proxy for the Pα luminosity (Figure 20, right). Again, the linear fit on all 132 HII knots is:

$$Log[L(8)] = (0.78 \pm 0.02) Log[L(24)] + (9.4 \pm 0.7). \quad (8)$$

The extrapolation of this relation to the 24 μm luminosity of the whole NGC 5194 would lead to an underestimate of its measured 8 μm dust luminosity by a factor $\sim$5.1.

In all cases (Figures 17–20), the integrated luminosity for the Inner Region is measured on the local background–subtracted images. The integrated 24 μm and 8 μm emission is 14% and 57%, respectively, larger than the sum of the individual HII knots. The 24 μm emission is thus almost entirely concentrated in the HII knots, with a small excess due to the faint knots discarded from our sample. Conversely, about a third of the 8 μ emission is outside the knots. This 'diffuse' emission is highly concentrated along filaments and is not the result of insufficient background subtraction.

The use of the extinction–corrected (and intrinsically mildly extinction–impacted) Pα has a large effect on the slopes of equations (4)–(7). For instance, use of the uncorrected Hα luminosity instead of the Pα would change the slope of equation (7) to (0.95 ± 0.05), very close to unity (see, also, Dale et al. 2005). Even in the absence of extinction corrections, a correlation between any of the above infrared luminosities and L(Hα) is preserved, owing to the fact that more actively star forming regions are also more extincted (Figure 13). However, absent or insufficient extinction corrections will have the effect of artificially increasing the slope between the infrared luminosity and the recombination line luminosity.

8. Discussion

The large wavelength range and the detailed spatial scale covered by the present body of observations of NGC 5194 has enabled a detailed investigation of the strenghts and limitations of various SFR indicators, and of the impact of dust obscuration on measurements of such indicators.

8.1. The Impact of Dust Obscuration

8.1.1. The Observed Trends

Quiescently star–forming galaxies do not follow the IR/UV–UV colors of starburst galaxies (Buat et al. 2002; Bell 2002; Gordon et al. 2004; Kong et al. 2004; Buat et al. 2005; Seibert et al. 2005): they tend to cover a much broader range in IR/UV at fixed UV color, spreading

towards lower IR/UV values than starbursts.

We recover a similar trend in the IR/UV–UV colors plane for individual HII knots ($\sim$500 pc in diameter) within a single star–forming galaxy. The knots show a much broader trend in the IR/FUV–UV colors plane than starbursts, and the latter form an 'upper envelope' to the knots (Figure 9, see also Bell et al. 2002). Analysis of various photometric and color characteristics of the knots shows that the broad spread ($\sim$1 dex peak–to–peak) is likely due to a spread in age of the UV–emitting population(s), between 2 and $\lesssim$100 Myr. None of the investigated knots, each encompassing $\sim$500 pc, can be thought of as containing a single age population. Most do contain multiple age populations, with the young population component responsible for ionizing the gas being, in many cases, spatially and temporally separated from the dominant UV–emitting population.

The general trends observed in Figure 9 and Figure 13 are still driven by effects of dust reddening and opacity: more opaque objects are in general redder and more actively star forming. This had already been established for starburst galaxies (Heckman et al. 1998) and for quiescently star–forming galaxies (Wang & Heckman 1996), and still holds true for individual star–forming knots within a single galaxy. It is a straightforward consequence of the Kennicutt–Schmidt law, plus (for galaxy samples) the mass–metallicity relation.

van der Hulst et al. (1988) had already established for NGC 5194 that the dust extinction affecting the clumped ionized gas is consistent with foreground dust, by comparing the Hα/radio ratio with the Balmer decrement. We confirm these earlier results, by finding a range of A_V from Hα/Pα which is similar to the range found by van der Hulst et al. (1988) from Hα/radio. Regions that are completely dust–buried are rare in this galaxy; of the 166 regions selected at 24 μm, only 2 were not detected in Hα. The vast majority of HII knots has detectable Hα, suggesting that: (1) presence of high extinctions does not imply large fractions of completely obscured (optical) emission (van der Hulst et al. 1988; James et al. 2004), and (2) timescales for newly formed cluster to separate from the parental cloud ($\sim$1–3 Myr, Garmany, Conti & Chiosi 1982; Leisawitz & Hauser 1988) are shorter than the evolution timescale of the cluster itself.

The opacity of the stellar continuum appears to be reasonably well described by a starburst–like opacity curve with $A_V^{star} \lesssim 0.44\ A_V^{gas}$ (Figures 10 and 11, e.g., Calzetti 2001), modulo the age–dependence of the observed UV luminosities and colors. The most extincted regions have UV attenuations corresponding to $A_V^{star} \sim 1.2$ mag, implying $A_V^{gas} \sim 2.8$ mag (Figure 10). This is consistent with the maximum value $A_V^{gas} \sim 3.5$ mag derived for the ionized gas (Figure 11).

Local peaks in the 8 μm and 24 μm emission usually correspond to local peaks in Hα,

and for 87% of the cases also to local peaks in the UV emission, albeit often displaced from the IR/Hα peaks. This spatial correspondence has led us to treat dust heating by UV photons as a local effect, for the most part circumscribed within the size of our apertures.

The decrease of the median A_V with galactocentric distance is quite typical of spiral galaxies (Peletier & Willner 1992; Giovanelli et al. 1995; Jones, Davies & Trewhella 1996; James et al. 2004, e.g.,). The increasing scatter as a function of distance from the nucleus shows that there are large local variations in the gas density, but the median gas extinction decreases from about 3.5 mag in the center to 2 mag at a distance of 3 kpc. We hypothize that the trend towards bluer UV colors for larger galactocentric distances (Figure 14) is mainly driven by dust reddening, although a trend towards younger ages for more distant UV–emitting knots is also contributing (Figure 15 and next section).

However, the characteristics of the knots' UV emission (Figures 9 and 10) imply that, unlike starburst galaxies, there is not a 1–to–1 correlation between the IR/FUV ratio and dust opacity or between the UV colors and dust reddening. In each case, an assumption on the mean age of the population dominanting the UV emission needs to be made. For instance, the opacity in the FUV, A(FUV) ranges between 4 mag and 6 mag in the center and between 0 mag and 1 mag at 13 kpc distance, for stellar populations in the age range 100-5 Myr. Our range of UV opacity values is larger, especially in the central regions, than what found by Boissier et al. (2004) from a radial analysis of NGC 5194 using FOCA data. FOCA's 2000 Å mean wavelenght is reasonably close to the GALEX NUV's mean wavelenght, allowing direct comparisons. Those authors find that the central NUV opacity in NGC 5194 is closer to 2 mag, about half of what we infer. Two reasons could explain the discrepancy: (1) we use HII knots, rather than azimuthally averaged information, thus excluding potentially less extincted diffuse emission; (2) Boissier et al. (2004) use the IR/NUV ratio as a tracer of UV dust opacity; this assumption will lead to underestimates of the UV opacity if, as we have seen in this work, the IR–dominating and UV–dominating populations do not coincide and show significant age differences.

The separation between IR–emitting and UV–emitting populations is particularly evident along the spiral arms, where about 1/2 of the HII knots show a displacement, at our resolution, between the IR (and Hα) peak and the UV peak within our apertures (Figure 4), and the IR (and Hα) emission is generally comparatively brighter than the UV emission along the inner edge, and fainter than the UV along the outer edge. This can be interpreted as the youngest stellar populations to be preferentially located along the inner edge of the spiral arms.

8.1.2. A 'Dust–Star Geometry' Scenario for Star–Forming Galaxies

Why are the opacity properties of NGC 5194, and probably of other star–forming galaxies, different from those of starbursts? A qualitative scenario involves the much higher SFR density (SFR per unit area), and the consequent presence of stronger mechanical feedback, in starbursts than in star–forming galaxies.

In starbursts, the feedback action of massive star winds and supernovae explosions is likely to eject large fractions of the gas and dust from the starburst volume into the surrounding interstellar medium. This will 'expose' the starburst population, that, in addition to ionize the gas and heat the dust, will also be responsible for the observed UV emission. In more quiescently star forming galaxies, the various HII regions/complexes are generally unconnected, implying a broader range of, and typically less strong, impact from feedback mechanisms. The most active HII complexes will still shed their dust cocoons via the action of gas outflows, thus resembling mini-starbursts, but increasingly less active HII regions will come out of the parental dust cloud only through secular motions. This last process takes time ($\sim$1–3 Myr, Garmany, Conti & Chiosi 1982; Leisawitz & Hauser 1988) and delays the emergence of the young population, which in the meantime will have aged. As a result, the UV–emitting populations in quiescently star–forming galaxies are not only 'old' ($\gg$12-15 Myr) and mostly non–ionizing, but also show a wide range of ages, which may depend on the local gas, dust, and star–formation conditions (Parravano, Hollenbach & McKee 2003). The ionizing stellar populations, conversely, remain for the most part sufficiently obscured by dust as to not provide the dominant UV contribution.

Our definition of 'old', however, is relative: the UV emission is still emerging from populations that are <100 Myr old in NGC 5194, and thus trace the 'recent', albeit not the 'current', star formation. This characteristic may question the use of the b parameter for measuring the degree of deviation of a star forming galaxy from the locus of starbursts in the IR/UV–UV colors plane (Kong et al. 2004). The observed parameters of NGC 5194, log[L(IR)/L(FUV)]=0.76 and β_{GLX}=$-$0.84 (where β_{GLX} is defined in Kong et al. (2004)), would place this galaxy among those with $b \lesssim 0.3$ according to the models of Kong et al. (2004, their Figure 4). However, the current to past star formation rate ratio in NGC 5194 is $b \gtrsim 2$, based on a 24 μm–derived SFR=3.4 $M_\odot$ yr^{-1} and a 2MASS H–band derived stellar mass. The disagreement can be reconciled if a modified b parameter is used, namely the ratio of the current to recent (<100 Myr) star formation rate; in this case $b_{recent} \lesssim 0.6$–0.8, for UV–emitting populations of average age 50–100 Myr and conservative assumptions on the dust obscuration. Thus, the deviation of star–forming galaxies from the locus of starbursts in the IR/UV–UV colors plane could be driven by star formation over the last few hundred Myr, or a fraction of the Hubble time, rather than the Hubble–time averaged star formation.

What are the conditions of applicability of the starburst opacity curve (Calzetti, Kinney & Storchi–Bergmann 1994; Meurer, Heckman & Calzetti 1999; Calzetti 2001) in those cases, like distant galaxies, where only integrated light information is often available? NGC 5194 classifies as a star–forming galaxy, rather than a starburst, despite is relatively high SFR (3.4 $M_\odot$ yr^{-1}, about 10 times higher than the local starburst galaxy NGC5253, Calzetti et al. (2004)). Its SFR density is, however, 0.015 $M_\odot$ yr^{-1} kpc^{-2}, or about 10–100 times lower than some of the 'weakest' starbursts (Kennicutt 1998b; Heckman 2005). Although it is unclear at this stage where the exact transition for the applicability of the starburst opacity curve is, a SFR density $>1M_\odot$ yr^{-1} kpc^{-2} is safely within the regime where the curve was derived.

8.1.3. The 2200 Å Feature

The UV color properties of the NGC 5194 HII knots suggest that the 2200 Å extinction curve feature is much weaker in this galaxy than what is observed in our own Galaxy (section 6.1.2). This is a tantalizing result, as the 2200 Å feature is widespread in the Milky Way, and there is evidence that this feature is mostly due to absorption (Calzetti et al. 1995a). NGC 5194 has a metallicity at least as high as, and possibly higher than, our Galaxy, and a SFR only a factor $\lesssim$2 higher. A number of studies have pointed out that the intensity of star formation may play a larger role than metallicity in determining the presence or absence of the 2200 Å feature in galaxies (Gordon et al. 2003): starburst galaxies lack the feature, independently of metallicity (Calzetti, Kinney & Storchi–Bergmann 1994), and both in the Milky Way and SMC there are sighlines with extinction curves that deviate from the 'canonical' ones (Lequeux et al. 1982; Gordon & Clayton 1998; Valencic et al. 2003). The exact mechanism that may take place in the HII knots of NGC 5194 is not clear at this point, although there could be mechanisms other than star formation intensity able to modify the strenght of the 2200 Å feature in the extinction curve, some of which are at work in dense clouds in the Milky Way itself (Whittet et al. 2004).

8.2. Intrinsic Properties of HII 'Complexes' in NGC 5194

The intrinsic properties of the Hα–emitting regions in the center of NGC 5194 have been extensively discussed by Scoville et al. (2001), and will not be repeated here. We only note that our brightest Hα knot has extinction–corrected luminosity $\sim10^{40}$erg s^{-1}, not dissimilar from the brightest HII regions measured (at much higher resolution) in Scoville et al. (2001). The range of intrinsic Hα luminosities correspond to SFR densities between

3×10^{-3} $M_\odot$ yr^{-1} kpc^{-2} and 0.07 $M_\odot$ yr^{-1} kpc^{-2}, when averaged over our $\sim$500 pc apertures. Some regions are easily above the threshold for starbursts (see previous section), as their intrinsic sizes are smaller than our resolution–driven apertures.

The brightest Hα knot in our sample corresponds to a stellar mass $\approx2\times10^5$ $M_\odot$ (for a Kroupa (2001) IMF in the range 0.01–100 $M_\odot$) within the $\sim$500 pc enclosed by each knot. For comparison, the oldest ($\lesssim$100 Myr), UV–emitting populations correspond to masses of $\sim$6-8$\times10^7$ $M_\odot$, as inferred from their extinction–corrected U and B emission, implying stellar masses $\approx$300–400 times larger than in the brightest ionizing population, but still consistent with the typical stellar mass densities of spiral galaxies ($\approx$200 $M_\odot$ pc^{-2}). Because of their large masses, these UV–bright knots are likely blends of multiple recently formed star clusters. The intrinsic masses and sizes of HII regions in NGC 5194 are in the range 10^3–10^4 $M_\odot$ and a few tens of pc, respectively (Scoville et al. 2001). Tidal forces are very effective at disrupting such small clusters, and cluster lifetimes in NGC 5194 have been found to be $<10^8$ yr (Lamers, Gieles & Portegies Zwart 2005), well matched to the lifetimes we derive from the U$-$B colors (Figure 15, left). Cluster stars will hence drift out of our apertures and diffuse in the galaxy over timescales of $\approx$30 Myr, for an assumed space velocity of 10 km s^{-1}, which typical of OB stars in the Milky Way. Thus, after $\approx$100 Myr, the clusters will no longer contribute to the concentrated UV emission identified in our HII knots.

We observe a radial trend for the UV–emitting regions to be younger at larger galactocentric distances, even after correction for dust extinction; the oldest regions ($\lesssim$100 Myr) are located closest to the nucleus, and ages decrease down to $\sim$5–20 Myr at about 3 kpc distance (Figure 15). A trend of decreasing mean age with distance was already observed by Bianchi et al. (2005) for NGC 5194; they find, however, older ages (>300 Myr) than ours for the same range of galactocentric distances, as they do not correct their colors for the effects of dust extinction. We argue that the radial age trend we observe in Figure 15 is real, and not an effect of insufficient extinction correction. The U$-$B colors we use to estimate ages are only moderately sensitive to dust reddening. Larger extinction values, or steeper extinction curves would produce unphysically blue UV colors and high UV luminosities much before changing significantly U$-$B–estimated ages (Figure 12 left). One possible interpretation is that, as dust extinction and local pressure increase towards the center, later and later ages become the dominant contributors to the observed UV emission, as younger populations remain deeply embedded in dust for comparatively longer times relative to their outer region's counterparts.

8.3. Star Formation Rate Indicators

8.3.1. The Infrared Luminosities

The analysis of the HII knots within the central 6 kpc of NGC 5194 shows tight correlations between the Pα luminosity and a variety of integrated and monochromatic infrared luminosities, confirming that in the dusty environment of this galaxy more strongly star–forming regions have larger infrared luminosities. Since the extinction–corrected Pα is a close tracer of current SFR, we can discuss our results in light of their relevance for tracing SFR.

As already stressed in many previous papers (for a few recent ones, see Kennicutt 1998a; Helou 2000; Kewley et al. 2002), the integrated 3–1100 μm luminosity, L(IR), is a reasonable tracer of SFR in galaxies. We confirm this result for individual HII knots in the dusty environment of NGC 5194, although we observe a mildly significant deviation from linearity (L(IR)$\propto$L(Pα)$^{(0.90\pm0.07)}$). The infrared emission longward of $\sim$50 μm can receive substantial contribution from large grains heated by a variety of stellar populations field (Helou 1986; Boulanger et al. 1988), including those that are no longer young and ionizing. This may be the case for the less strongly star–forming HII knots in our sample, whose infrared emission may receive comparatively higher contamination from the non–ionizing populations present in our apertures, thus driving the exponent towards values smaller than one.

The closest tracer of SFR in NGC 5194 is the monochromatic luminosity L(24), on the local scales of the HII knots. We find a linear correspondence between L(24) and the Pα luminosity, L(24)$\propto$L(Pα)$^{(1.03\pm0.04)}$. This implies that the very small grains responsible for the IR emission closely trace the young ionizing stars (Cesarsky et al. 1996; Helou 2000; Haas, Klaas & Bianchi 2002; Helou et al. 2004). We have quantified this correlation to have a dispersion of a factor 2.5–3 peak–to–peak in the center of NGC 5194, where metallicity variations from region to region can be expected to be small (Zaritsky, Kennicutt & Huchra 1994), and where HII regions are located in a relatively uniform environment.

However, the use of L(24) as a general SFR indicator for galaxies should be regarded with caution at this stage. We have seen that the ratio L(24)/SFR changes by a factor of a few from galaxy to galaxy (Figure 19), at least when considering star–formation–dominated galaxies. Ionizing stars may heat the dust to different average 'effective temperatures', that may depend on the local galactic conditions. The resulting variations in the emerging infrared SEDs will imply variable fractions of L(24)/L(IR), hence L(24)/SFR, from galaxy to galaxy (Dale et al. 2001). Further, L(24) can be strong in galaxies dominated by nuclear non–thermal sources. In NGC 5194, the relatively faint nuclear non–thermal source represents only 2.2% of the 24 μm luminosity of the whole galaxy, and 6% of the 24 μm

luminosity within the central 6 kpc. For comparison, the extinction–corrected Pα luminosity of the nuclear source is about 4% of the integrated luminosity in the inner 6 kpc, thus $L(24)_{AGN}/L(24)_{InnerRegion} \approx 1.5$–2 $L(P\alpha)_{AGN}/L(P\alpha)_{InnerRegion}$; this implies that L(24) is moderately overluminous relative to L(Pα) in dusty and gas–rich non–thermal sources. In light of all the above, analysis of a large sample of galaxies is needed to constrain the galaxy–to–galaxy variation of L(24)/SFR, and establish whether this luminosity can be effectively used as a SFR tracer.

The monochromatic 8 μm luminosity is more diffuse than either the hydrogen recombination line emission and the 24 μm luminosity. L(8) correlates tightly with L(Pα), but with a significant non–linearity, $L(8) \propto L(P\alpha)^{(0.79\pm0.02)}$. The emission in the 8 μm and other MIR bands is attributed to Polycyclic Aromatic Hydrocarbons (PAH, Leger & Puget (1984)), large molecules transiently heated by single UV and optical photons (Sellgren, Luan & Werner 1990), and which can be destroyed, fragmented, or ionized by harsh UV photon fields (Boulanger et al. 1988, 1990; Helou, Ryter & Soifer 1991; Pety et al. 2005). Spitzer data of the nearby galaxy NGC300 show, indeed, that the 8 μm emission highlights the rims of HII regions and is depressed inside the regions (Helou et al. 2004). The analysis of M33 by Hinz et al. (2005) shows that high intensity radiation fields destroy the PAH (see, also, e.g. Helou, Ryter & Soifer 1991; Contursi et al. 2000). In addition, dust–poor environments are ineffective at shielding the carriers from destruction by the UV emission (Boselli, Lequeux & Gavazzi 2004), and the PAH emission nearly disappears in galaxies with metallicities below $\sim$25% solar (Engelbracht et al. 2005b).

The non–linear correlation between L(8) and the hydrogen recombination lines, also found by Peeters, Spoon & Tielens (2004) in the Milky Way, suggests that a second mechanism in addition to star formation is responsible for the heating of the 8 μm carriers. The 'second mechanism' can indeed be a combination of multiple mechanisms, including dissociation or ionization of the PAH molecules in correspondence of regions of intense star formation (Tacconi–Garman et al. 2004), and heating of the 8 μm dust by the UV photons in the general radiation field (Li & Draine 2002; Haas, Klaas & Bianchi 2002; Boselli, Lequeux & Gavazzi 2004), possibly from B stars (Peeters, Spoon & Tielens 2004).

It is perhaps premature to generalize the above result, obtained locally within galaxies, to galaxies as a whole. For instance, Roussel et al. (2001) and Förster Schreiber et al. (2004) find a linear relation between the PAH emission and the hydrogen recombination line emission in a sample of local galaxies (see, however, Boselli, Lequeux & Gavazzi 2004). More analysis is clearly needed to ascertain the conditions under which the MIR PAH emission might be used as a SFR indicator.

8.3.2. The UV Luminosity

Only ∼40% of the detected UV light from the Inner Region's HII knots is from 'young' systems, where 'young' is defined as any region with intrinsic UV and U−B colors typical of a ≤30 Myr old cluster. Less than half of the observed UV emission comes from currently star forming regions, and the rest is associated with recent past (last ≈50–100 Myr) star formation. This questions the use of the UV emission for measuring *current* SFRs in 'normal' star–forming galaxies, in addition to complicate attempts to remove effects of dust opacity from the observed UV light.

The application of attenuation–correction techniques like, e.g., the starburst opacity curve, to the observed UV emission of star–forming galaxies may lead to overcorrections of the UV emission, due to the extraneous contribution from the evolved populations, and overestimates of the SFR(UV) (Buat et al. 2002). For instance, if the 'red' UV color of NGC 5194 were interpreted as due to dust reddening only, and the starburst opacity curve applied 'as is', the resulting A(FUV)=2.8 mag would lead to SFR(FUV)∼13 $M_\odot$ yr^{-1}, using Kennicutt (1998a)'s formula and a Kroupa (2001) IMF. This is about a factor of 4 higher than what derived from the 24 μm luminosity. When the presence of populations as old as ∼50–100 Myr is accounted for, A(FUV)∼1.6 mag, corresponding to a mean SFR(FUV)∼4.3 $M_\odot$ yr^{-1}, only about 30% higher than SFR(24 μm). This discrepancy stresses the difference between normal star–forming and starburst galaxies. For starbursts, mechanical feedback is likely to be strong enough that the observed UV light traces the same population responsible for the gas ionization and dust heating; hence, one can expect SFR(FUV)∼SFR(line)∼SFR(IR). Conversely, in normal star–forming galaxies the observed UV light traces evolved, non–ionizing populations, and the relation between SFR(FUV) and SFR(line) or SFR(IR) will depend on the recent star formation history (see, also, Kong et al. 2004).

9. Summary and Conclusions

The multiwavelength analysis of NGC 5194 using a combination of Spitzer, GALEX, HST, and ground–based data has yielded new information on the properties of dust opacity and star formation in this galaxy.

The impact of dust is large on the observed properties of the HII knots, ranging from A_V ∼3.5 mag in the center to A_V ∼0–1 mag in the outskirts of this galaxy, as derived from both the ionized gas emission and the stellar continuum UV emission. The trend of decreasing extinction for increasing galactocentric distance is common among spiral galaxies. Somewhat unexpectedly, though, we don't find evidence for a strong 2200 Å feature in the

extinction curve of NGC 5194, a feature that is instead ubiquitous in our own Milky Way.

We reproduce, for individual HII knots, the broadening in the IR/UV–UV color plane observed for normal star–forming galaxies. The deviation from the starburst opacity curve is due to age effects: the UV–emission of the knots traces evolved stellar populations, with the oldest ones (∼50–100 Myr) being further away from the locus of the starburst opacity curve. In terms of spatial location, some of the oldest UV–emitting regions are located near the center of the galaxy, within ∼1 kpc of the nucleus. We also find evidence for HII knots along the outer edge of spiral arms to be more evolved (less ionizing) than the HII knots along the inner edges.

The UV emission in normal star forming galaxies does not trace *current star formation*, but the *recent* one. In this respect, the parametrization of the deviation from the starburst curve with the 'b' parameter (Kong et al. 2004) may be inadequate, as the relevant quantity for measuring such deviation is not the ratio of the current to the Hubble time–averaged star formation but the current to the recent (<100 Myr in NGC 5194) star formation. In addition, dust extinction corrections developed for starburst galaxies will fail, by factors of a few, to recover the intrinsic UV emission from normal star–forming galaxies, due to the contribution to the UV emission from non–star–forming populations in the latter galaxies. Although it is unclear how to separate starbursts from star–forming galaxies at high redshifts, where only spatially integrated quantities are often accessible, a method involving the SFR density may offer a useful discriminant. In particular, the validity of the starburst opacity curve has been tested on starbursts in the SFR density range ∼1–50 $M_\odot$ yr^{-1} kpc^{-2}.

The most accurate *local* tracer of current SFR in NGC 5194 is the 24 μm emission, which shows a linear correlation with nebular line emission, with a peak–to–peak dispersion of a factor 2.5–3. However, the L(24)/SFR ratio, although constant within the central region of NGC 5194, varies by a factor of a few from galaxy to galaxy. Thus, the use of L(24) as a SFR tracer for galaxies in general is premature, until further investigation with larger samples of galaxies.

Conversely, the monochromatic 8 μm luminosity of the HII knots does not show a linear correlation with the nebular gas emission. The 8 μm emission is overluminous relative to the galaxy's average for weakly ionized regions, and underluminous for strongly ionized regions. A combination of two effects, heating of the carriers by the general radiation field and ionization/destruction/fragmentation in hard UV radiation field, may explain the observed trend (Haas, Klaas & Bianchi 2002; Boselli, Lequeux & Gavazzi 2004; Peeters, Spoon & Tielens 2004; Tacconi–Garman et al. 2004).

The conclusions reached so far are based on a single galaxy. In the case of L(24)

and L(8), these luminosities need to undergo further scrutiny to gauge galaxy–to–galaxy variations, and test their applicability as SFR tracers in galaxy samples. The SINGS sample of local star–forming galaxies is optimally designed to address this issue in the near future.

This work is part of SINGS, The Spitzer Infrared Nearby Galaxies Survey, one of the Spitzer Space Telescope Legacy Science Programs, and was supported by the JPL, Caltech, Contract Number 1224667. The Spitzer Space Telescope is operated by JPL, CalTech, under NASA Contract 1407. The SINGS team acknowledges the hard work by the IRAC, MIPS, and IRS instrument teams and the Spitzer Science Center for making possible the work presented here.

GALEX (Galaxy Evolution Explorer) is a NASA Small Explorer, launched in April 2003. Bianchi, Madore, Martin (PI), and Thilker gratefully acknowledge NASA's support for construction, operation, and science analysis for the GALEX mission, developed in cooperation with the Centre National d'Etudes Spatiales of France and the Korean Ministry of Science and Technology.

DC and RCK gratefully acknowledge the hospitality of the Aspen Center for Physics (Aspen, Colorado), where some parts of this work were developed by the authors during the Summer 2004 Workshop on Star Formation.

REFERENCES

Barger, A.J., Cowie, L.L., & Richards, E.A. 2000, AJ, 119, 2092

Bell, E.F. 2002, ApJ, 577, 150

Bell, E.F., Gordon, K.D., Kennicutt, R.C., & Zaritsky, D. 2002, ApJ, 565, 994

Bianchi, L., Thilker, D., Burgarella, D., Friedman, P., Hoopes, C., Boissier, S., Gil de Paz, A., Barlow, T., Byun, Y.–I., et al. 2005, ApJ, 619, L71

Bianchi, L., et al. 2004a, in The Local Group as and Astrophysical Laboratory, STScI May Symposium, eds. M. Livio et al.

Bianchi, L., Madore, B., Thilker, D., Gil de Paz, A., and the GALEX Team 2004b, AAS, 203, 91.12

Boissier, S., Boselli, A., Buat, V., Donas, J., & Milliard, B. 2004, A&A, 424, 465

Boselli, A., Lequeux, J., & Gavazzi, G. 2004, A&A, 428, 409

Bouchet, P., Lequeux, J., Maurice, E., Prevot, L., & Prevot-Burnichon, M. L. 1985, A&A, 149, 330

Boulanger, F., Beichmann, C., Desert, F.–X., Helou, G., Perault, M., & Ryter, C. 1988, ApJ, 332, 328

Boulanger, F., Falgarone, E., Puget, J.L., & Helou, G. 1990, ApJ, 364, 136

Bresolin, F., Garnett, D.R., & Kennicutt, R.C. 2004, ApJ, 615, 228

Buat, V., Boselli, A., Gavazzi, G., & Bonfanti, C. 2002, A&A, 383, 801

Buat, V., et al. 2005, ApJ, 619, L51

Calzetti, D. 2001, PASP, 113, 1449

Calzetti, D., Armus, L., Bohlin, R.C., Kinney, A.L., Koornneef, J., & Storchi-Bergmann, T. 2000, ApJ, 533, 682

Calzetti, D., Bohlin, R.C., Kinney, A.L., Storchi–Bergmann, T., & Heckman, T.M. 1995a, ApJ, 443, 136

Calzetti, D., Bohlin, R.C., Gordon, K.D., Witt, A.N., & Bianchi, L. 1995b, ApJ, 446, L97

Calzetti, D. Harris, J., Gallagher, J.S., Smith, D.A., Conselice, C.J., Homeier, N., & Kewley, L. 2004, AJ, 127, 1405

Calzetti, D., Kinney, A.L., & Storchi–Bergmann, T. 1994, ApJ, 429, 582

Calzetti, D., Kinney, A.L., & Storchi–Bergmann, T. 1996, ApJ, 458, 132

Cardelli, J.A., Clayton, G.C., & Mathis, J.S. 1989, ApJ, 345, 245

Cesarsky, D., Lequeux, J., Abergel, A., Perault, M., Palazzi, E., Madden, S., & Tran, D. 1996, A&A, 315, L309

Chapman, S.C., Blain, A.W., Ivison, R.J., & Smail, I.R. 2003, Nature, 422, 695

Chapman, S.C., Smail, I., Windhorst, R., Muxlow, T., & Ivison, R.J. 2004, ApJ, 611, 732

Charlot, S., & Fall, S.M. 2000, ApJ, 539, 718

Conselice, C.J., Bershady, M.A., Dickinson, M.E., & Papovich, C. 2003, AJ, 126, 1186

Contursi, A., Lequeux, J., Cesarsky, C., Boulanger, F., Rubio, M., Hanus, M., Sauvage, M., Tran, D., Bosma, A., Madden, S., & Vigroux, L. 2000, A&A, 362, 310

Dale, D.A., & Helou, G. 2002, ApJ, 576, 159

Dale, D.A., Helou, G., Contursi, A., Silbermann, N.A., & Kolhatkar, S. 2001, ApJ, 549, 215

Dale, D.A., et al. 2005, submitted

Desert, F.–X., Boulanger, F., & Puget, J.L. 1990, A&A, 237, 215

Engelbracht, C.W., et al. 2005a, in prep.

Engelbracht, C.W., et al. 2005b, in prep.

Erb, D.K., Shapley, A.E., Steidel, C.C., Pettini, M., Adelberger, K.L., Hunt, M.P., Moorwood, A.F.M., & Cuby, J.–G. 2003, ApJ, 591, 101

Ford, H.C., Crane, P.C., Jacoby, G.H., Lawrie, D.G., & van der Hulst, J.M. 1985, ApJ, 293, 132

Förster Schreiber, N.M., Roussel, H., Sauvage, M., & Charmandaris, V., 2004, A&A, 419, 501

Garmany, C.D., Conti, P.S., & Chiosi, C. 1982, ApJ, 263, 777

Giavalisco, M., Dickinson, M., Ferguson, H.C., Ravindranath, S., Kretchmer, C., Moustakas, L.A., Madau, P., Fall, S.M. Gardner, J.P., et al. 2004, ApJ, 600, L103

Giovanelli, R., Haynes, M.P., Salzer, J.J., Wegner, G., da Costa, L.N., & Freudling, W., 995, AJ, 110, 1059

Goad, J.W., & gallagher, J.S., III 1985, ApJ, 297, 98

Goldader, J.D., Meurer, G,, Heckman, T.M., Seibert, M., Sanders, D.B., Calzetti, D., & Steidel, C.C. 2002, ApJ, 568, 651

Gordon, K.D., & Clayton, G.C., 1998, ApJ, 500, 816

Gordon, K.D., Clayton, G.C., Misselt, K.A., Landolt, A.U., & Wolff, M.J. 2003, ApJ, 594, 279

Gordon, K.D., Perez–Gonzalez, P.G., Misselt, K.A., Murphy, E.J., Bendo, G.J., Walfer, F., Thornely, M.D., Kennicutt, R.C., et al. 2004, ApJS154, 215

Gordon, K.D., Rieke, G.H., Engelbracht, C.W., Muzerolle, J., Stanberry, J.A., Misselt, K.A., Morrison, J.E., Cadien, J., et al., 2005, PASP, in press (astroph/0502080)

Haas, M., Klaas, U., & Bianchi, S. 2002, A&A, 385, L23

Heckman, T.M. 1999, in After the Dark Ages: When Galaxies were Young, S. Holt & E. Smith eds., AIPC 470, 322

Heckman, T.M. 2005, in Starbursts: from 30 Doradus to Lyman Break Galaxies, R. de Grjis & R.M. Gonzalez Delgado eds., in press (astroph/0502022)

Heckman, T.M., Robert, C., Leitherer, C., Garnett, D.R., & van der Rydt, F. 1998, ApJ, 503, 646

Helou, G. 1986, ApJ, 311, L33

Helou, G. 2000, in Infrared Astronomy: Today and Tomorrow, eds. F. Casoli, J. Leuquex, & F. David (Springer=–Verlag: Les Ulis), 337

Helou, G., Khan, I.R., Malek, L., & Boehmer, L. 1988, ApJS, 68, 151

Helou, G., Ryter, C., & Soifer, B.T. 1991, ApJ. 376, 505

Helou, G., Roussel, H., Appleton, P., Frayer, D., Stolovy, S., Storrie–Lombardi, L., Hurst, R., Lowrance, P., et al. 2004, ApJS, 154, 253

Hill, J.K., Waller, W.H., Cornett, R.H., Bohlin, R.C., Cheng, K.–P., Neff, S.G., O'Connell, R.W., Roberts, M.S. et al. 1997, ApJ, 477, 673

Hinz, J.C., et al. 2005, in prep.

Hoopes, C.G., & Walterbos, R.A.M. 2003, ApJ, 586, 902

James, P.A., Shane, N.S., Knapen, J.H., Etherton, J., & Percival, S.M. 2004, A&A, in press (astroph/0410386).

Jones, H., Davies, J.I., & Trewhella, M. 1996, MNRAS, 283, 316

Kauffmann, G., Heckman, T.M., White, S.M., Charlot, S., Tremonti, C., Brinchmann, J., Bruzual, G., Peng, E.W., et al. 2003, MNRAS, 341, 33

Kennicutt, R.C. Jr. 1998a, ARA&A, 36, 189

Kennicutt, R.C. Jr. 1998b, ApJ, 498, 541

Kennicutt, R.C., Armus, L., Bendo, G., Calzetti, D., Dale, D.A., Draine, B.T., Engelbracht, C.W., Gordon, D.A., et al. 2003, PASP, 115, 928

Kennicutt , R.C. Jr., Edgar, B.K., & Hodge, P.W. 1989, ApJ, 337, 761

Kennicutt, R.C. Jr. et al. 2005, in prep.

Kewley, L.J., Geller, M.J., Jansen, R.A., & Dopita, M.A. 2002, AJ, 124, 3135

Kong, X., Charlot, S., Brinchmann, J., & Fall, S.M. 2004, MNRAS, 349, 769

Kroupa, P. 2001, MNRAS, 322, 231

Laird, E.S., Nandra, K., Adelberger, K.L., Steidel, C.C., & Reddy, N.A. 2005, MNRAS, 359, 47

Lamers, H.J.G.L.M., Gieles, M., & Portegies Zwart, S.F. 2005, A&A, 429, 173

Leger, A., & Puget, J.L. 1984, A&A, 137, L5

Leitherer, C., Schaerer, D., Goldader, J.D., González Delgado, R.M., Robert, C., Kune, D.F., de Mello, D.F., Devost, D., & Heckman, T.M. 1999, ApJS, 123, 3

Leisawitz, D., & Hauser, M.G. 1988, ApJ, 332, 954

Lequeux, J., Maurice, E., Prevot-Burnichon, M.-L., Prevot, L., & Rocca-Volmerange, B. 1982, A&A, 113, L15

Li, A., & Draine, B.T. 2002, ApJ, 572, 232

Martin, D.C., et al. 2005, ApJ, 619, L1

McQuade, K., Clzetti, D., & Kinney, A.L. 1995, ApJS, 97, 331

Meurer, G.R., Heckman, T.M., & Calzetti, D. 1999, ApJ, 521, 64

Osterbrock, D.E., 1989, Astrophysics of Gaseous Nebulae and Active Galactic Nuclei (Mill Valley (CA): University Science Books)

Pahre, M.A., Ashby, M.L.N., Fazio, G.G., & Willner, S.P. 2004, ApJS, 154, 229

Parravano, A., Hollenbach, D.J., & McKee, C.F. 2003, ApJ, 584, 797

Peeters, E., Spoon, H.W.W., & Tielens, A.G.G.M. 2004, ApJ, 613, 986

Peletier, R.F., & Willner, S.P. 1992, AJ, 103, 1761

Pety, J., Teyssier, D., Fosse‘, D., Gerin, M., Roueff, E., Abergel, A., Habart, E., & Cernicharo, J. 2005, A&A, in press (astroph/0501339)

Reddy, N.A., & Steidel, C.C. 2004, ApJ, 603, L13

Regan, M.W., Thornley, M.D., Bendo, G.J., Draine, B.T., Li, A., Dale, D.A., Engelbracht, C.W., Kennicutt, R.C., et al. 2004, ApJS, 154, 204

Rosa–Gonzalez, D., Terlevich, E., & Terlevich, R. 2002, MNRAS, 332, 283

Roussel, H., Sauvage, M., Vigroux, L., & Bosma, A. 2001, A&A, 372, 427

Seibert, M. et al. 2005, ApJ, 619, L55

Sellgren, K., Luan, L., & Werner, M.W. 1990, ApJ, 359, 384

Scoville, N.Z., Polletta, M., Ewald, S., Stolovy, S.R., Thompson, R., & Rieke, M. 2001, AJ, 122, 3017

Smail, I., Ivison, R.J., Owen, F.N., Blain, A.W., & Kneib, J.-P. 2000, ApJ, 528, 612

Steidel, C.C., Adelberger, K.L., Giavalisco, M., Dickinson, M.E., & Pettini, M. 1999, ApJ, 519, 1

Sturm, E., Lutz, D., Verma, A., Netzer, H., Sternberg, A., Moorwood, A.F.M., Oliva, E., & Genzel, R. 2002, A&A, 393, 821

Tacconi–Garman, L.E., Sturm, E., Lehnert, M., Lutz, D., Davies, R.I., & Moorwood, A.F.M. 2004, A&A, in press (astroph/0411272)

Terashima, Y., & Wilson, A.S. 2001, ApJ, 560, 139

Thilker, D.A., Walterbos, R.A.M., raun, R., & Hoopes, C.G. 2002, AJ, 124, 3118

Trentham, N., Kormendy, J., & Sanders, D.B. 1999, AJ, 117, 2152

Tully, R.B. 1988, Nearby Galaxies Catalog, (Cambridge: CUP)

Valencic, L.A., Clayton, G.C., Gordon, K.D., & Smith, T.L. 2003, ApJ, 598, 369

van der Hulst, J.M., Kennicutt, R.C., Crane, P.C., & Rots, A.H. 1988, A&A, 195, 38

Wang, B., & Heckman, T.M. 1996, ApJ, 457, 645

Whittet, D.C.B., Shenoy, S.S., Clayton, G.C., & Gordon, K.D. 2004, ApJ, 602, 291

Williams, G.G., Olszewski, E., Lesser, M.P., & Burge, J.H. 2004, SPIE, 5492, 787

Witt, A.N., & Gordon, K.D. 2000, ApJ, 528, 799

Zaritsky, D., Harris, J., Thompson, I.B., & Grebel, E.K. 2004, AJ, 128, 1606

Zaritsky, D., Kennicutt, R.C., Jr., & Huchra, J.P. 1994, ApJ, 420, 87

This preprint was prepared with the AAS LaTeX macros v5.2.

Fig. 1.— Two three–color composites of M51. **(Left)** The far–UV (blue), continuum–subtracted Hα (green), and 24 μm dust (red) emission of the galaxy pair. The FUV and FIR images, from GALEX and Spitzer, respectively, have closely–matched resolution ($\approx 6''$, while the resolution of the ground–based Hα image has been degraded to match that of the two space–borne images. **(Right)** The continuum–subtracted Hα (blue), 3.6 μm stellar continuum (green), and 8 μm dust (red) emission of the galaxy pair. This second image exploits the higher angular resolution of the IRAC images (about $2''$ FWHM) to provide higher level of detail. The stellar continuum emission traces evolved (old) stellar populations. In this figure, a foreground star appears pure green. North is up, East is left. The size of the pictures is $\sim 8'.6 \times 11'.8$.

Fig. 2.— The 24 μm MIPS image of NGC 5194 with 112 of the 166 apertures in which photometry has been performed overlayed as red circles. The 112 apertures are located in the Outer Region (see text). North is left, East down. The flux scale is logarithmic, with larger fluxes in darker grey. The areas where the local background has been measured for removal from the aperture fluxes are shown as rectangular outlines on the image; they are sequentially numbered 1 to 11, and the one corresponding to the entire Inner Region is marked IR. The linear sizes of the image are similar to those of Figure 1.

Fig. 3.— Images of the Inner Region (the central area imaged in Pα) are shown in the light of: continuum–subtracted Hα line emission (top–left), continuum–subtracted Pα line emission (top–right), dust–only IRAC 8 μm emission (bottom–left), and MIPS 24 μm emission (bottom–right). The North–East direction is indicated by vectors on the IRAC and MIPS images. 54 of the 166 apertures used for photometry are located in the Inner Region and are overlayed on the four images; they are sequentially numbered 1 through 54 on the MIPS24 image, with the Seyfert 2 nucleus indicated as aperture 1. The flux scale in each panel is logarithmic, with larger fluxes in darker grey. The linear size of each Inner Region image is $2'.46$, or $\sim$5.9 kpc.

Fig. 4.— A comparison of aperture locations on a small section of the the 24 μm **(left)** and FUV **(right)** images, showing the displacement between the IR and FUV peaks. Particularly obvious are the cases of apertures 07 and 08. The orientation of the images is the same as Figures 3.

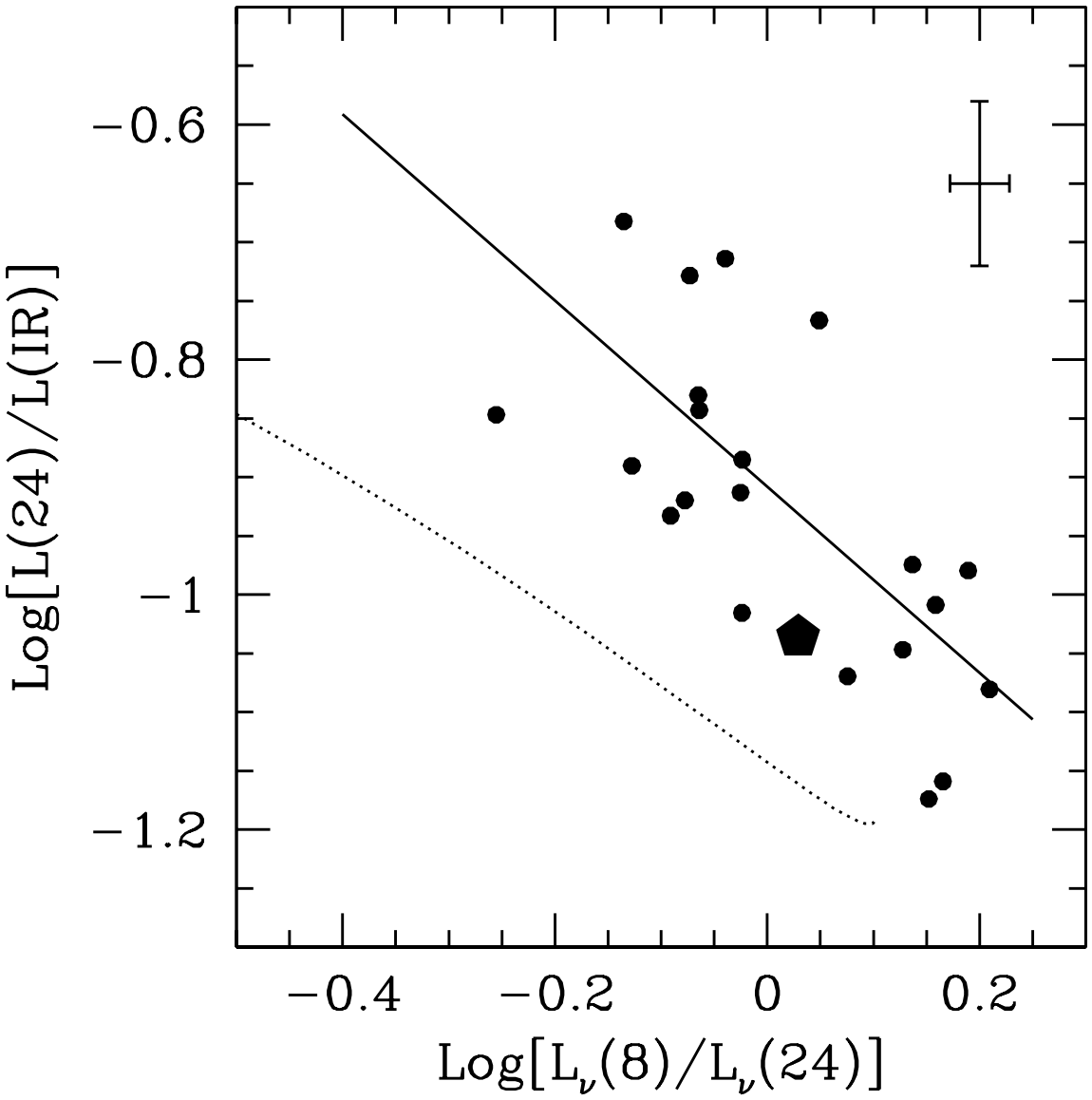

Fig. 5.— The 24 μm–to–total infrared luminosity as a function of the 8/24 μm flux ratio for 21 regions in the center and along the spiral arms of NGC 5194, where L(IR)=L(3–1100 μm) and L(24)=νL$_\nu$(24). The 21 regions have 70″ diameter, selected to properly sample the lowest resolution MIPS channel (see text). A representative error bar appropriate for the calibration uncertainties is shown at the top–right of the figure. The datapoints show a mild correlation in the plane defined by the two luminosity ratios, that we fit with a straight line (continuous line). For comparison, the location of the whole galaxy on this plane is shown as a large filled pentagon. Not surprisingly, the whole galaxy location is along the lower envelope of the locus defined by the HII knots. The prediction from the model of Dale & Helou (2002), appropriate for whole galaxies, is shown as a dotted line.

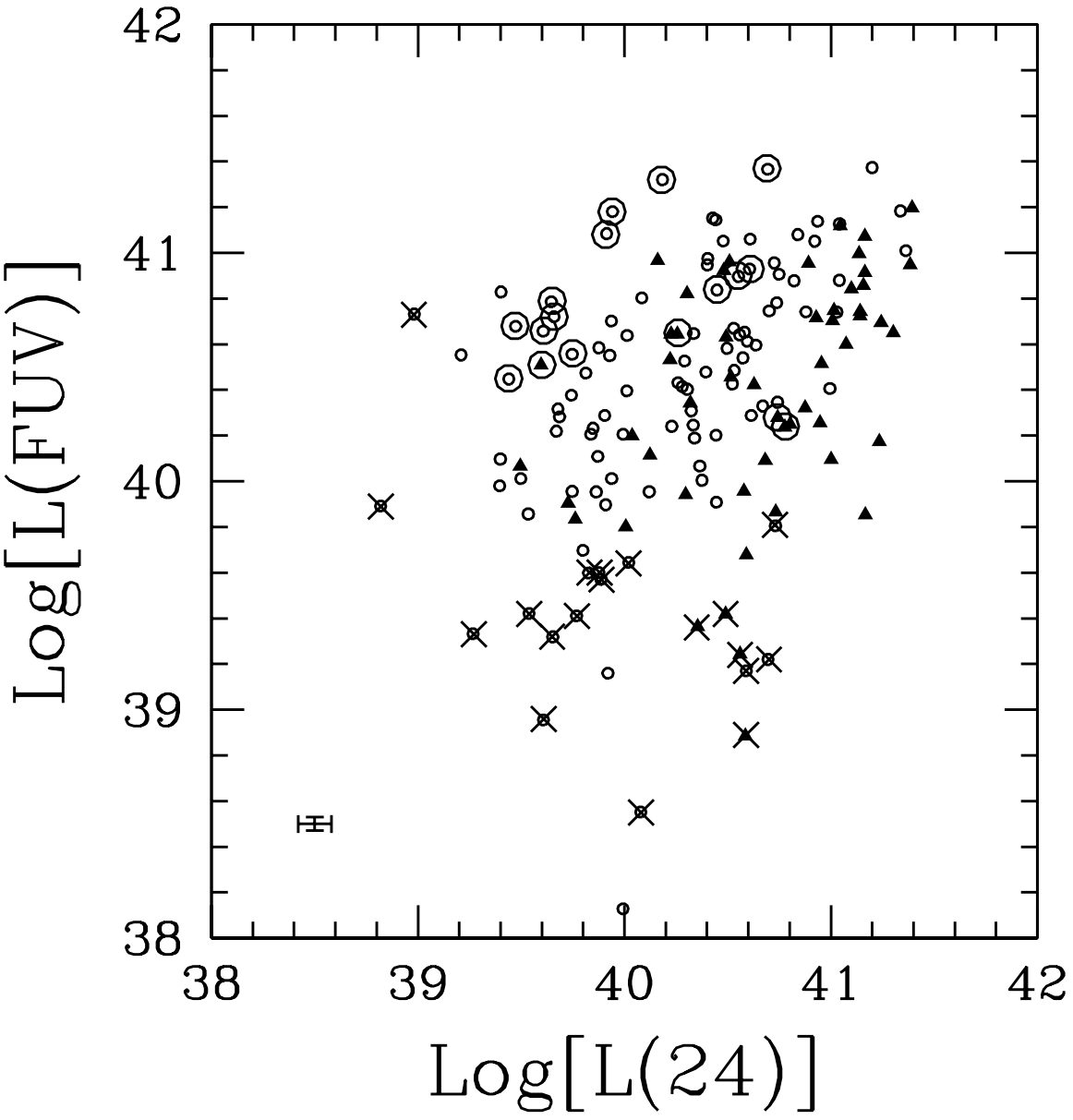

Fig. 6.— Observed IR and FUV luminosities for the 166 regions with aperture photometry. The IR is at 24 μm and the FUV is at 0.153 μm. Different symbols are used for apertures in the Inner Region (filled triangles) and the Outer Region (small empty circles). Most regions are IR–selected; the UV–selected regions are marked with large empty circles. Upper limits (see text) are indicated by crosses. The median error bar is shown at the left–bottom of the plot. HII knots in the Inner Region tend to have, on average, higher 24 μm luminosity than the Outer Region's knots, at fixed UV luminosity. Also, the UV luminosities span close to the full range at each fixed 24 μm luminosity, implying that there is no correlation between the two quantities.

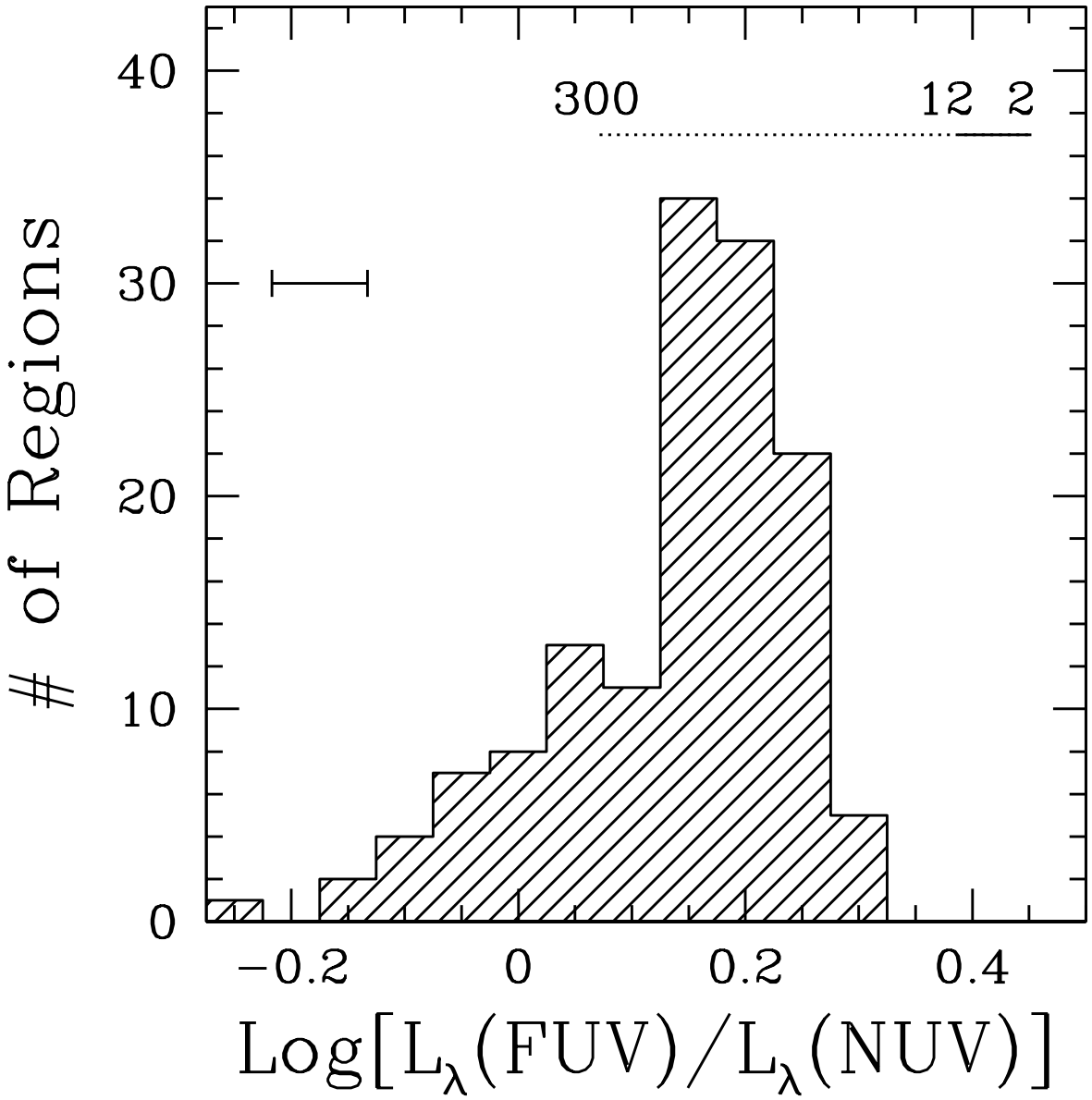

Fig. 7.— Histogram of the observed UV colors for the 132 regions with aperture photometry (upper limits are omitted). The UV color is the 0.153/0.231 μm flux ratio (GALEX FUV/NUV). The top–right horizontal bar indicates the intrinsic UV colors of dust–free, instantaneous–burst stellar populations for a range of ages (from Starburst99, Leitherer et al. 1999): 2–12 Myr (continuous line, ionizing population), and 12-300 Myr (dotted line, non–ionizing population). A median error bar on the colors is shown at the top–left of the plot. Noticebly, none of the observed HII knots has UV colors compatible with a dust–free, ionizing stellar population.

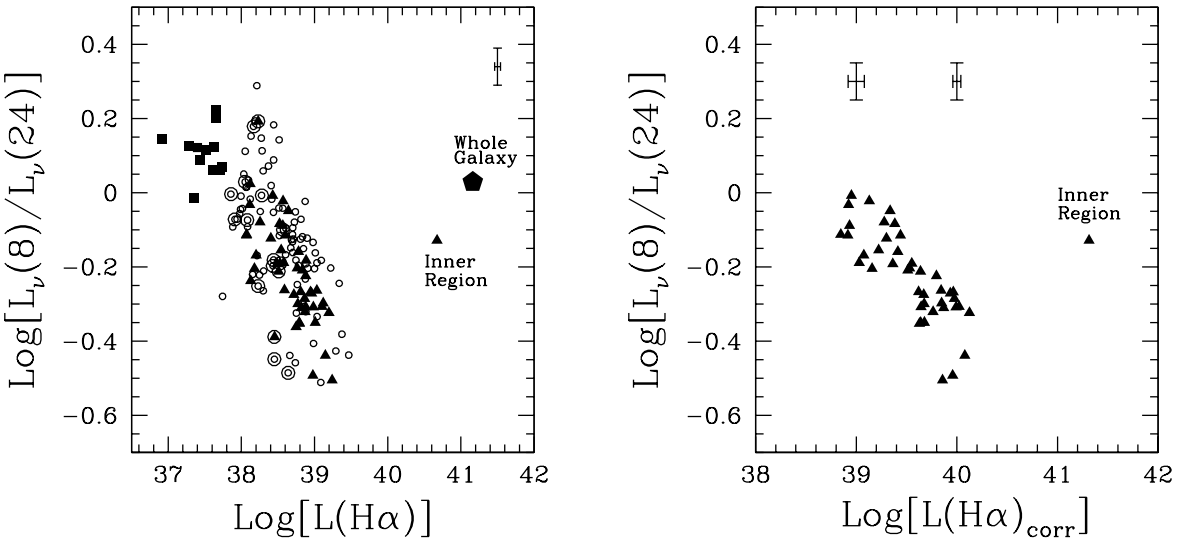

Fig. 8.— **(Left)** Observed IR colors as a function of the observed Hα luminosity, for both the HII knots in both the Inner (triangles) and Outer Regions (circles); the integrated colors for the Inner Region and the whole galaxy are shown as marked. For comparison, the infrared colors of the 12 background regions are shown as filled squares; the Hα luminosity of the backgorund regions is calculated over the 13″ diameter apertures also used for the HII knots. **(Right)** Observed IR colors as a function of the *extinction–corrected* Hα luminosity for the Inner Region. The symbols are the same as Figure 6. Upper limits have been omitted. Median error bars are shown in both plots.

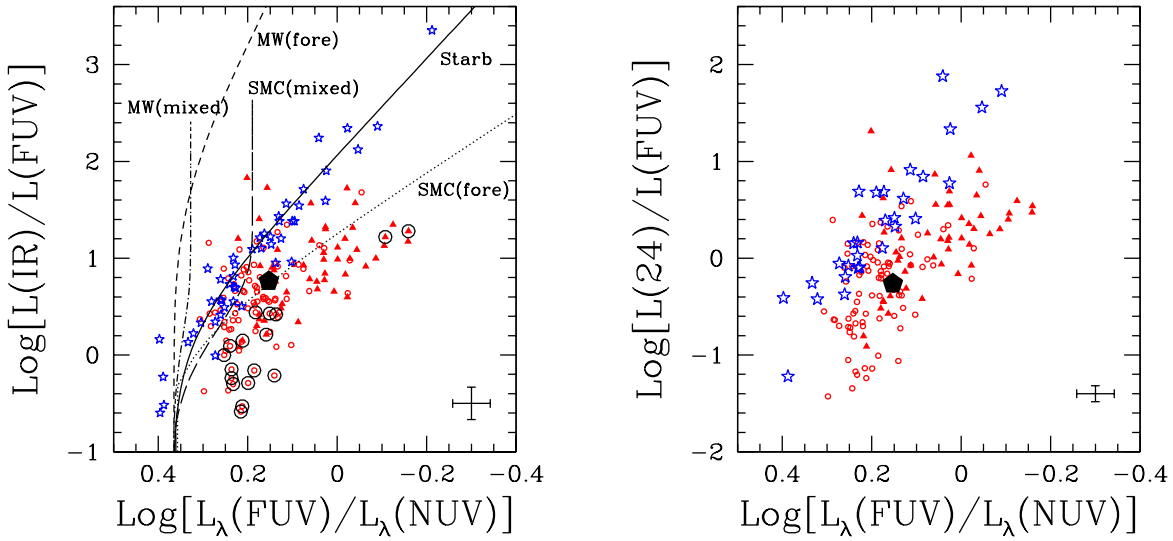

Fig. 9.— **(Left)** The total opacity, expressed as the infrared to FUV luminosity ratio, as a function of the observed UV colors. L(IR) and L(FUV) are total luminosities in the FIR and FUV, respectively (L(FUV)=λ L$_\lambda$(FUV)). Symbols are as in Figure 6. The filled pentagon is the position on the plot of the emission from the entire NGC 5194 galaxy. Data for 29 starburst galaxies from the sample of Calzetti, Kinney & Storchi–Bergmann (1994) are plotted as star symbols. Photometry for the starbursts has been performed on a galaxy–wise basis (the entire starburst region at UV wavelengths, from IUE, and the entire galaxy in the IR, from IRAS). Model lines are obtained by convolving the spectral energy distribution of a constant star formation stellar population (Leitherer et al. 1999) with a range of dust attenuation values and geometries: foreground, non–scattering dust screens (MW extinction curve: short dashed line; SMC extinction curve: dotted line), homogeneous mixtures of stars and dust (MW extinction curve: dot–dashed line; SMC extinction curve: long–dashed line), and the starburst dust distribution (continuous line, via the starburst opacity curve, Calzetti, Kinney & Storchi–Bergmann (1994); Meurer, Heckman & Calzetti (1999); Calzetti et al. (2000)). **(Right)** The same plot with the abscissa given as the L(24)–to–L(FUV) ratio. For the starbursts, the IRAS 25 μm flux is used as a close approximation of the MIPS 24 μm. For both plots, median error bars are shown.

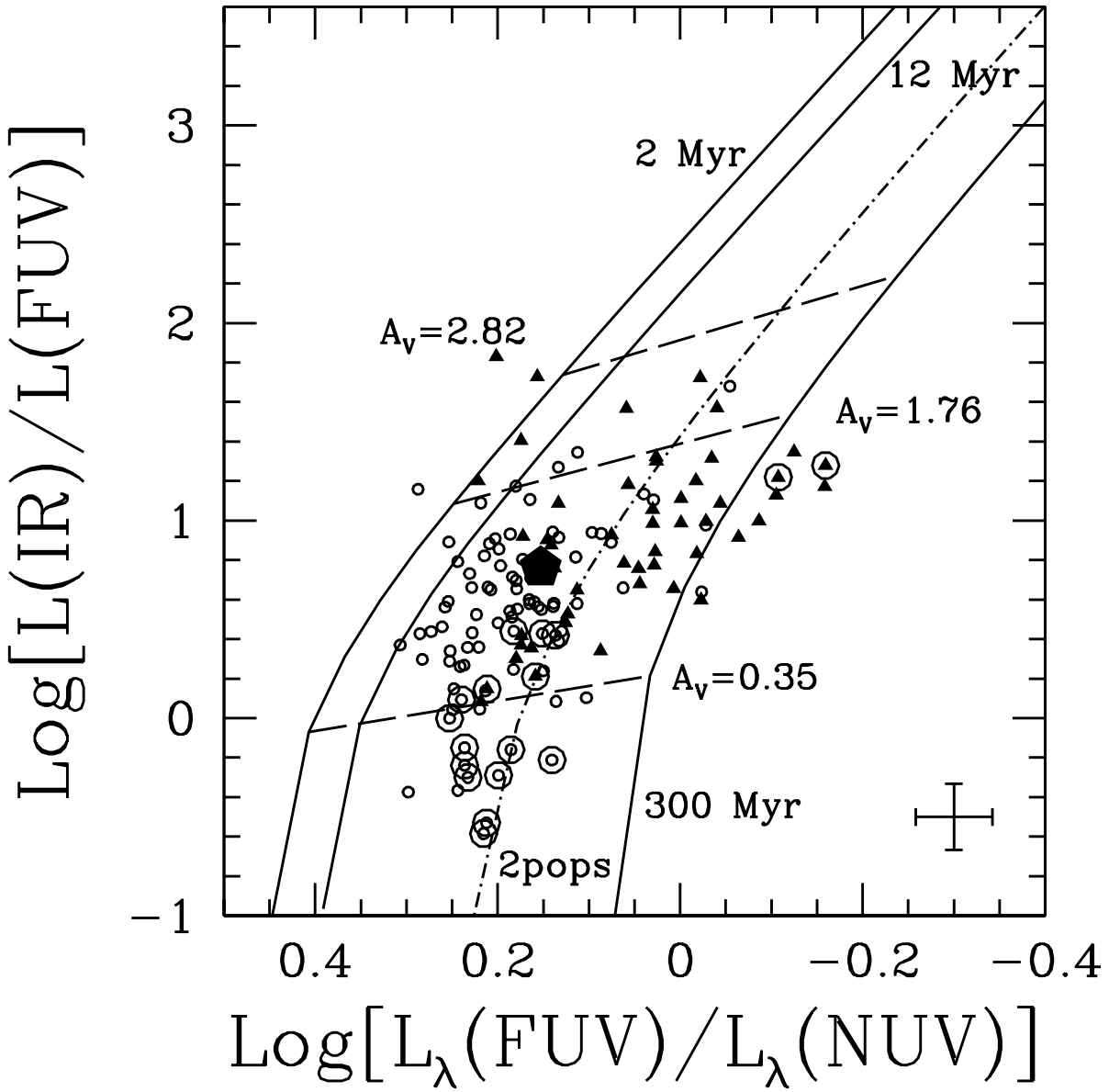

Fig. 10.— The same plot and HII knots datapoints as Figure 9, now compared to models of ageing burst populations convolved with the starburst opacity curve for increasing amount of dust attenuation. The continuous lines mark the locus of instantaneous burst populations, 2 Myr (left line), 12 Myr (center line), and 300 Myr old (right hand–side line), respectively. The dot–dashed line marked '2pops' shows the model track for the combination of a 5 Myr old instantaneous burst with a 300 Myr old one. The mass of the 5 Myr old burst is 300 times lower than than of the 300 Myr old one, and its extinction systematically higher by ΔA_V=0.25 mag (except at A_V=0, where both populations are extinction"free); both population models are convolved with the starburst opacity curve. More details are given in section 6.1.1. Loci of constant extinction A_V are marked by inclined dashed lines; these lines are not perfectly horizontal, implying that fixed IR/FUV ratios do not exactly correpond to fixed dust opacity A_V, in the presence of age variations. The vast majority of the HII–emitting knots in NGC 5194 are bracketed by models of stellar populations in the age range

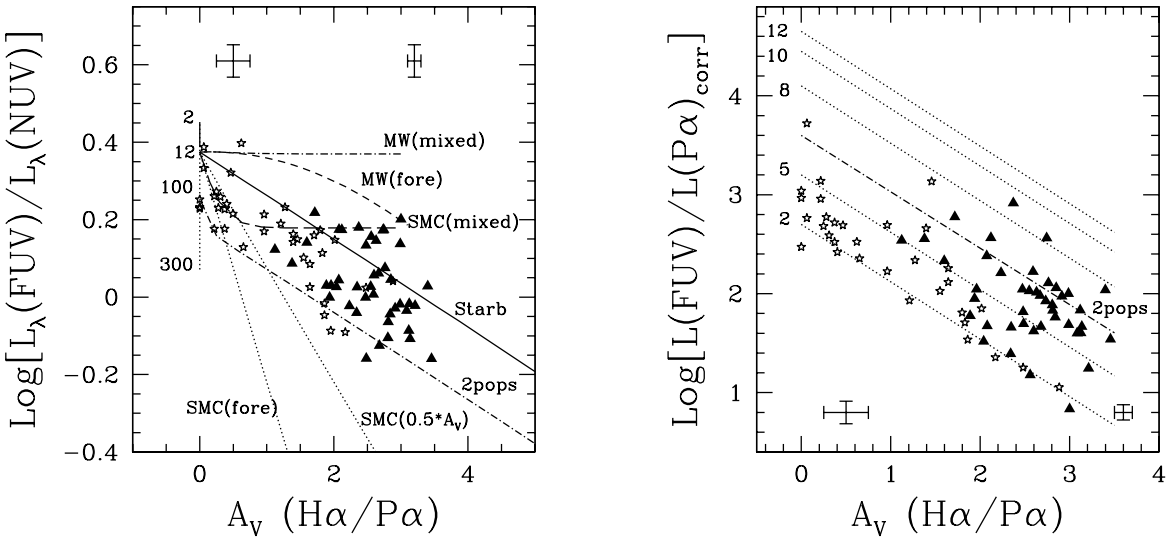

Fig. 11.— **(Left)** The UV flux ratio as a function of the optical extinction A_V, in mag, for 42 knots in the Inner Region (filled triangles). A_V is calculated from the observed Hα/Pα ratio, for a foreground dust screen. Star symbols identify the starburst galaxies. The vertical line at A_V=0 marks the range of intrinsic colors for gas–ionizing instantaneous burst populations (2–12 Myr, Leitherer et al. 1999, continuous line), and for non–ionizing populations up to 300 Myr (dotted line). Dust models are the same described in Figure 9 (left). One additional model shown here is an SMC foreground, non–scattering, clumpy screen, with the stellar continuum affected by half the reddening of the gas (dotted line marked SMC(0.5 A_V)). The dot-dashed line marked '2pops' represents the 2–populations model described in section 6.1.1 and Figure 10. The discontinuity at A_V=0.25 mag is a model artifact due to the different treatment of the two populations for A_V=0 mag (both populations are extinction–free) and A_V >0 mag (the younger population is systematically more extincted than the older population). Median error bars at the two extremes of the extinction range are shown on top of the plot; the uncertainties in A_V are mostly driven by the depth of the Pα image. **(Right)** The ratio of the FUV luminosity to the extinction–corrected Pα luminosity as a function of the extinction A_V. The datapoints, symbols, and the '2pops' model are as in the previous panel. For the starbursts, L(Pα) is derived from the extinction corrected Hα luminosity, and A_V is from the Hα/Hβ line ratio (Calzetti, Kinney & Storchi–Bergmann 1994). The intrinsic ratios for unreddened instantaneous burst populations are marked by an appropriate number (the age in units of Myr) at A_V=0. The dotted lines mark the extinction trend in the FUV using the starburst opacity curve.

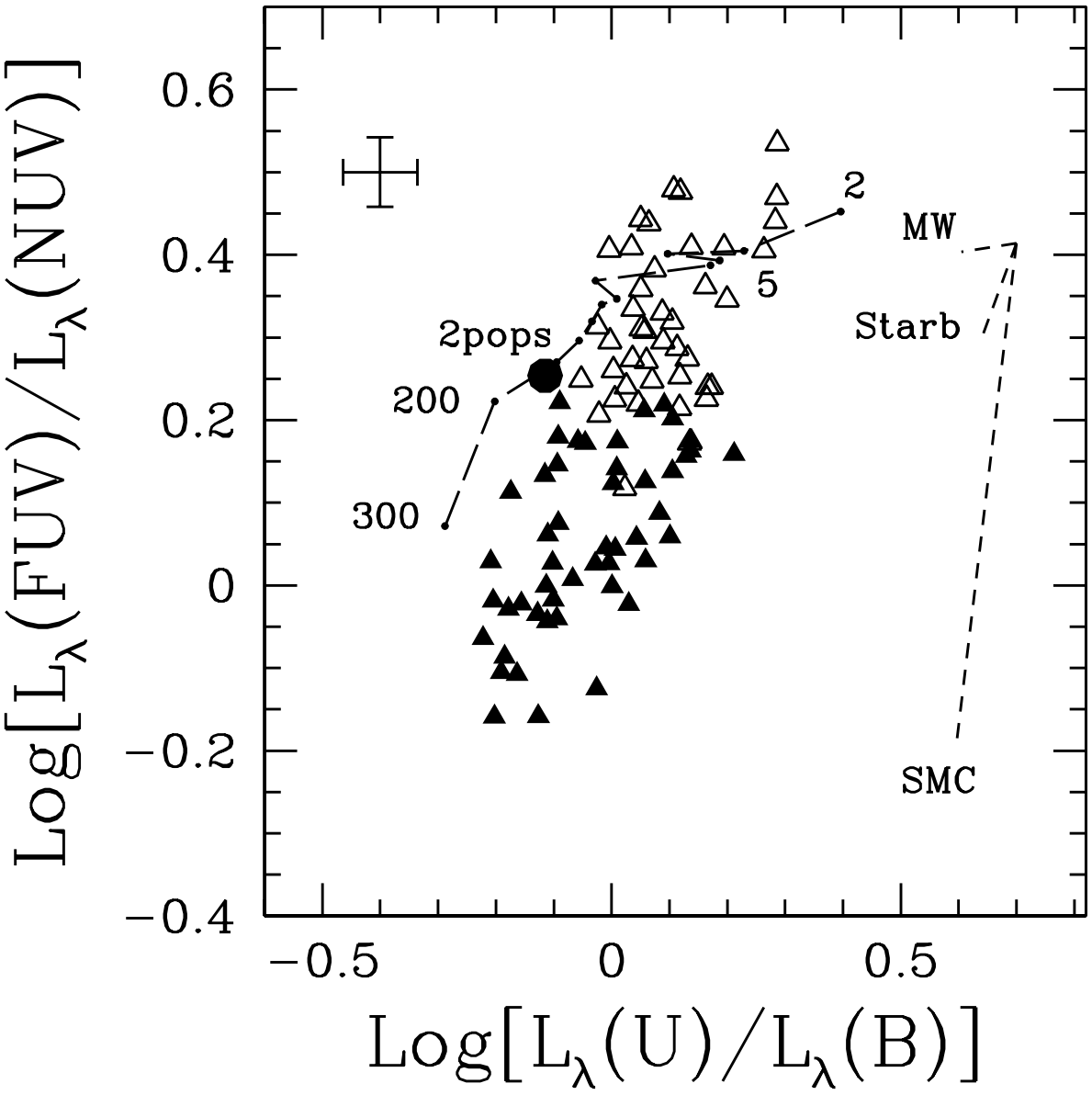

Fig. 12.— The UV colors as a function of U−B for the 42 HII knots in the Inner Region (filled triangles). U−B is expressed as the flux ratios in the two bands: $\mathrm{Log}[L_\lambda(U)/L_\lambda(B)]$. The empty triangles are the extinction–corrected colors, using the starburst opacity curve and the appropriate A_V for each knot (Figure 11). The color evolution of ageing instantaneous bursts between 2 and 300 Myr are shown as a long–dashed line, with a few representative ages indicated in Myr. The large filled circle shows the extinction–free colors of the 2–populations model described in Figure 10 and section 6.1.1. Short–dashed straight lines show the effect on the colors of 1 mag extinction at V for Galactic (MW), starburst (Starb), and Small Magellanic Cloud (SMC) reddening curves.

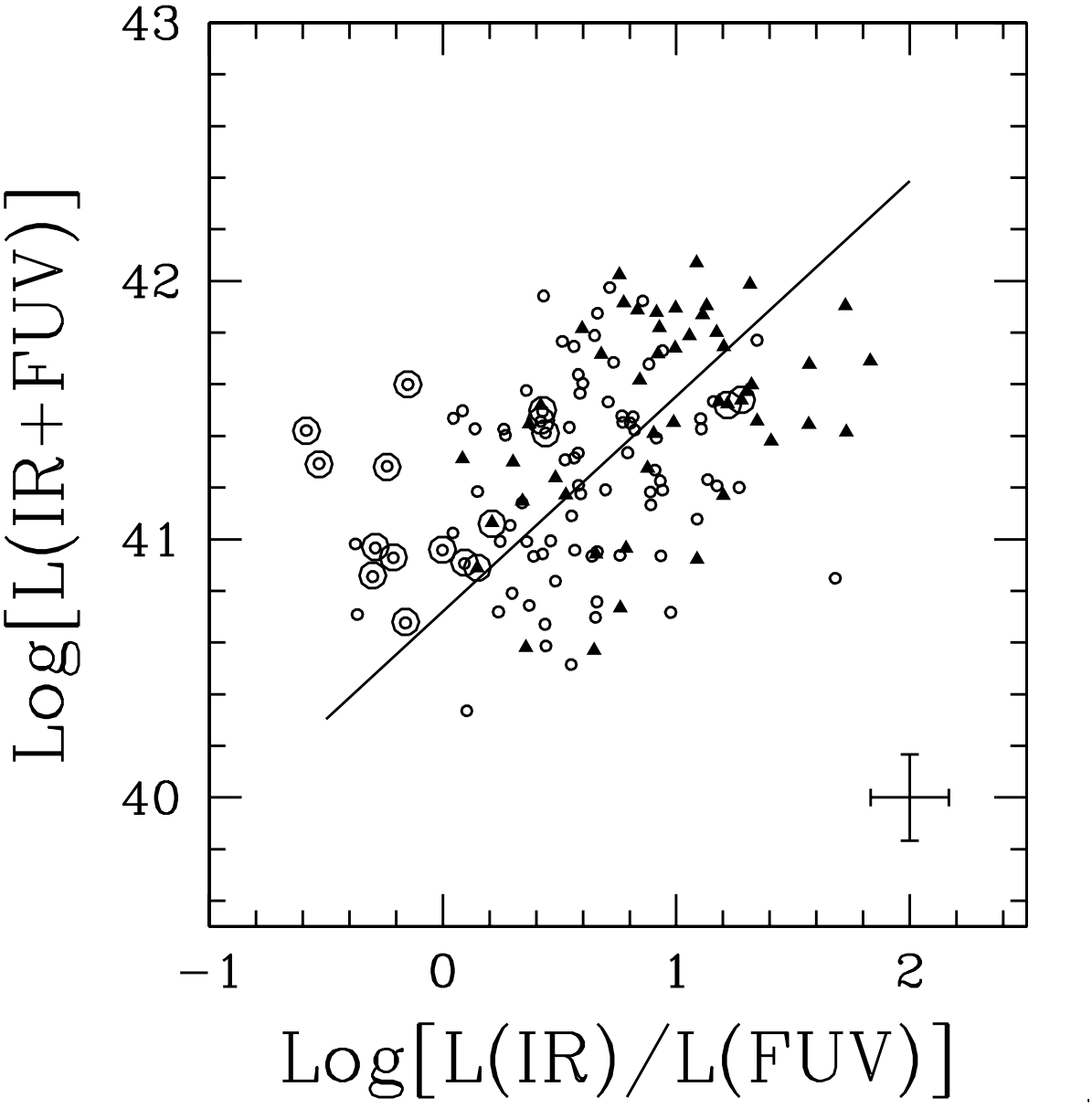

Fig. 13.— The sum of the infrared and FUV luminosities as a function of infrared-to-FUV ratio. Symbols are as in Figure 6. The sum of the IR and FUV emission is a proxy for total UV emission, and star formation rate, in starburst galaxies (Heckman et al. 1998). In NGC 5194 the datapoints show some correlation (5.1 σ significance). The continuous line is from the best fit to starburst galaxies of Heckman et al. (1998), shifted along the vertical axis by a factor $\sim$40 to account for the lower luminosity of HII knots relative to galaxies.

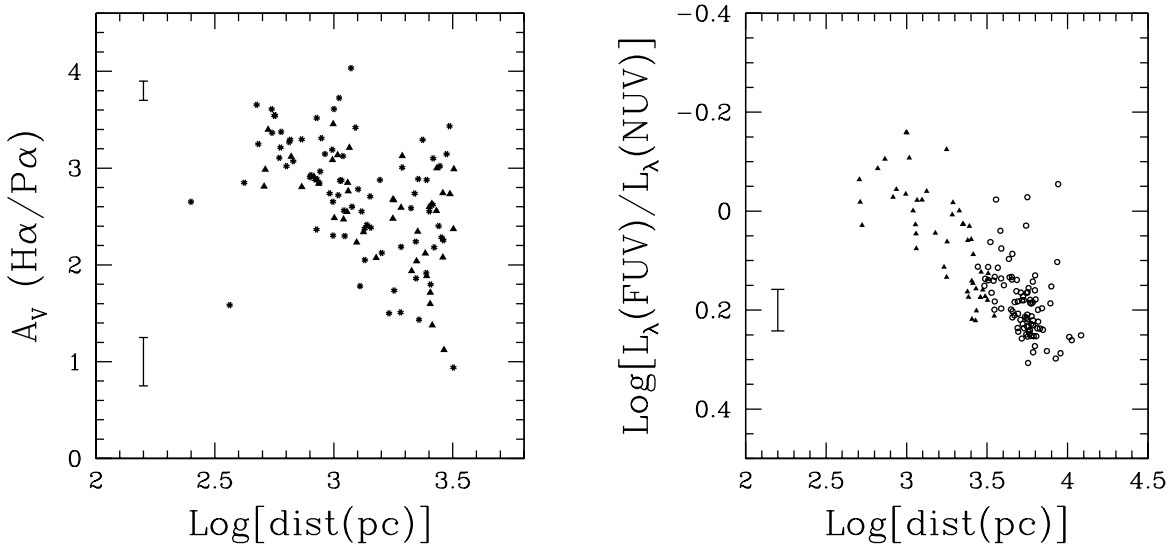

Fig. 14.— **(Left)**. The extinction at V, A_V, in magnitudes, as a function of the distance from the galaxy's nucleus, from ∼300 pc to 3.1 kpc. Data are shown for measurements performed in the 13″–diameter apertures (filled triangles) and the 4″–diameter apertures (asterisks). The two asterisks closest to the nucleus show a strong deviation (low A_V values) from the general trend; the low A_V values are consistent with those measured in the active nucleus itself. The same 'dip' is not measured in the larger aperture data, as the closest datapoint to the nucleus (excluding the nucleus itself) is over 500 pc away. **(Right)**. The same plot for the observed UV colors, up to ∼13 kpc distance from the nucleus.

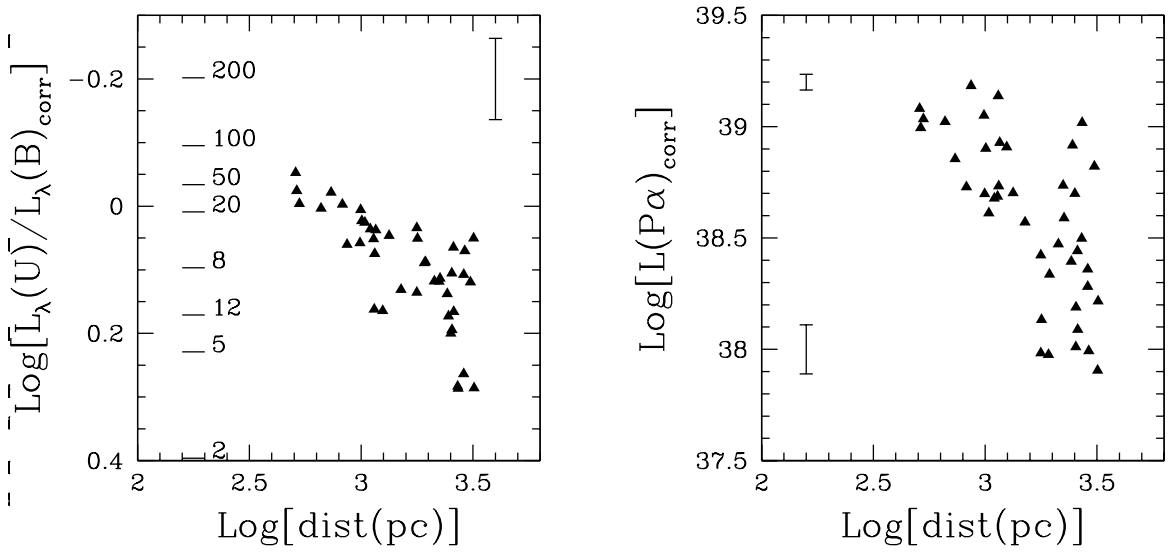

Fig. 15.— The *extinction–corrected* $L_\lambda(U)/L_\lambda(B)$ color **(left)** and the extinction–corrected Pα luminosity **(right)** as a function of the distance from the galaxy's nucleus, for the Inner Region. The expected colors of instantaneous burst populations are shown as horizontal marks on the left diagram, marked by their age (in Myr). The median uncertainties are shown in both plots as vertical bars. The intrinsic colors of the UV–detected knots show a trend for younger ages further away from the nucleus, while at the same time the same regions show more massive young populations being present closer to the nucleus.

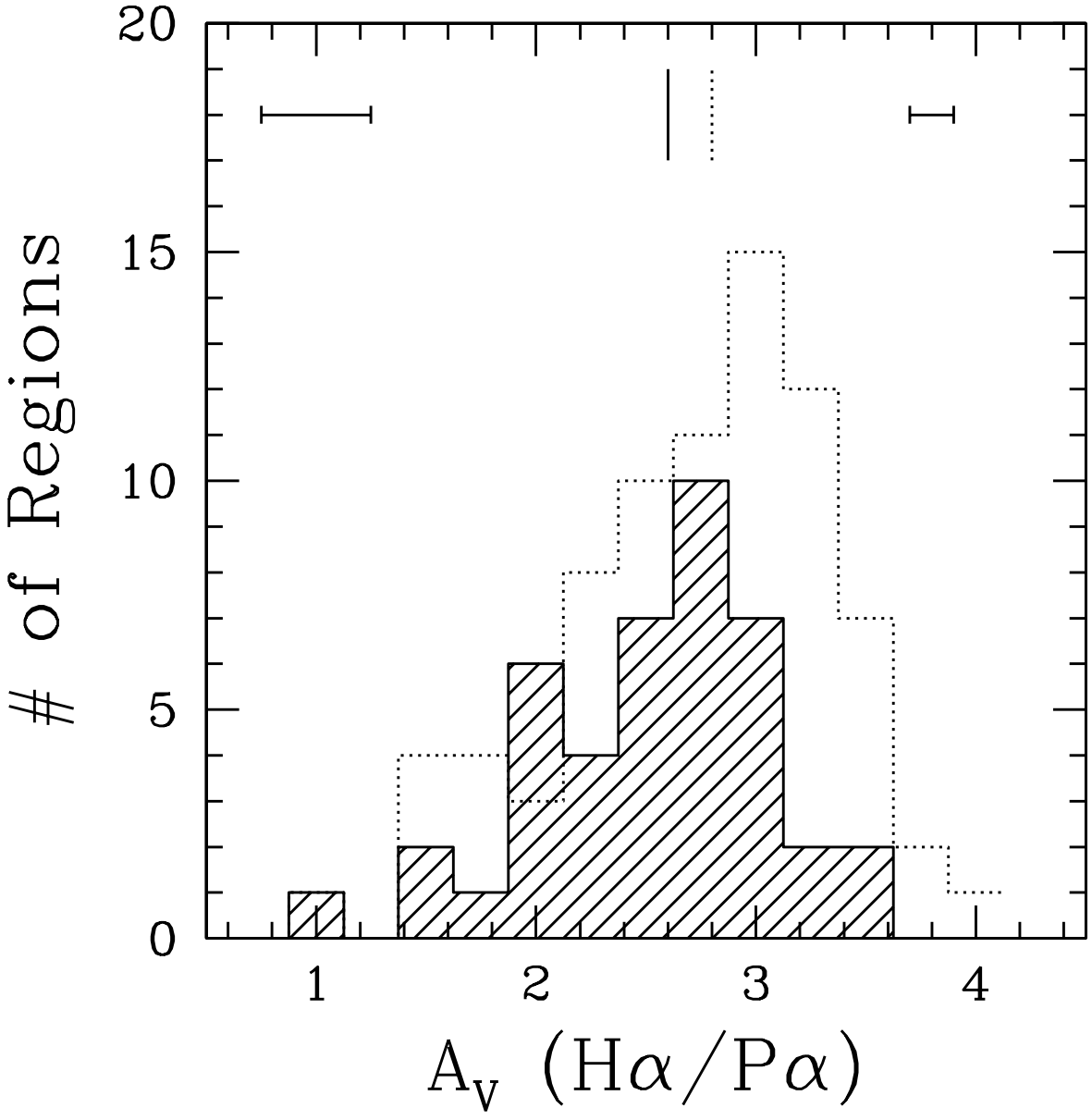

Fig. 16.— Histogram of the extinction A_V for the 42 13″–diameter regions (shaded histogram) and for the 78 4″–diameter regions (dotted histogram). The median values of the two distributions, $A_V \simeq$2.6 mag and 2.8 mag, respectively, are shown as vertical bars at the top of the diagram. The uncertainties in A_V are shown as horizontal error bars.

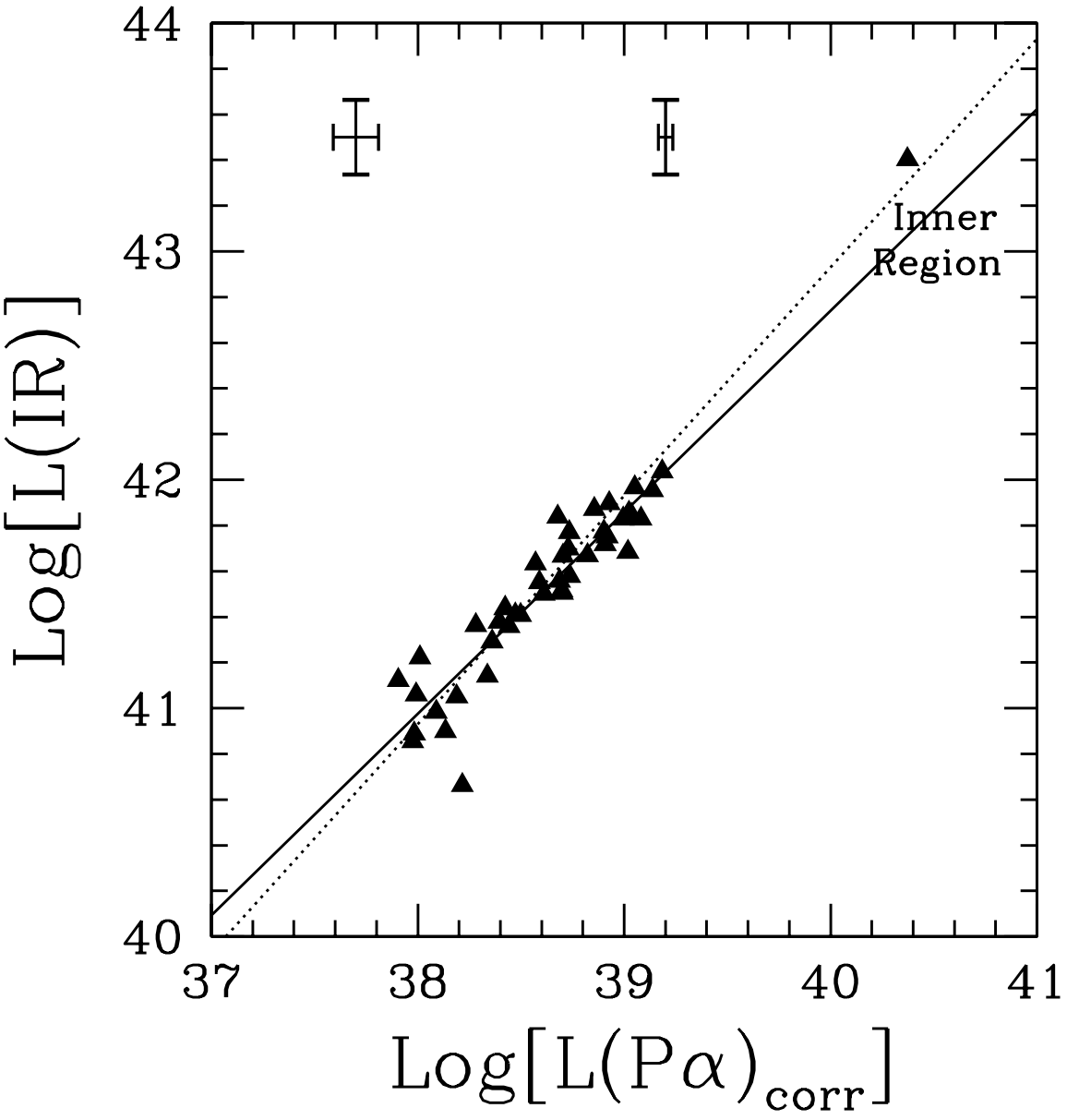

Fig. 17.— The infrared luminosity as a function of the extinction–corrected Pα luminosity for the 42 knots in the Inner Region. The best fit line to the HII knots and the luminosity relation with slope unity are shown as a continuous line and a dotted horizontal line, respectively. The location on the plot of the integrated light (background–subtracted) from the Inner Region is also shown, and identified with its name. Median error bars are shown at the two extremes of the Pα luminosity range for the HII knots.

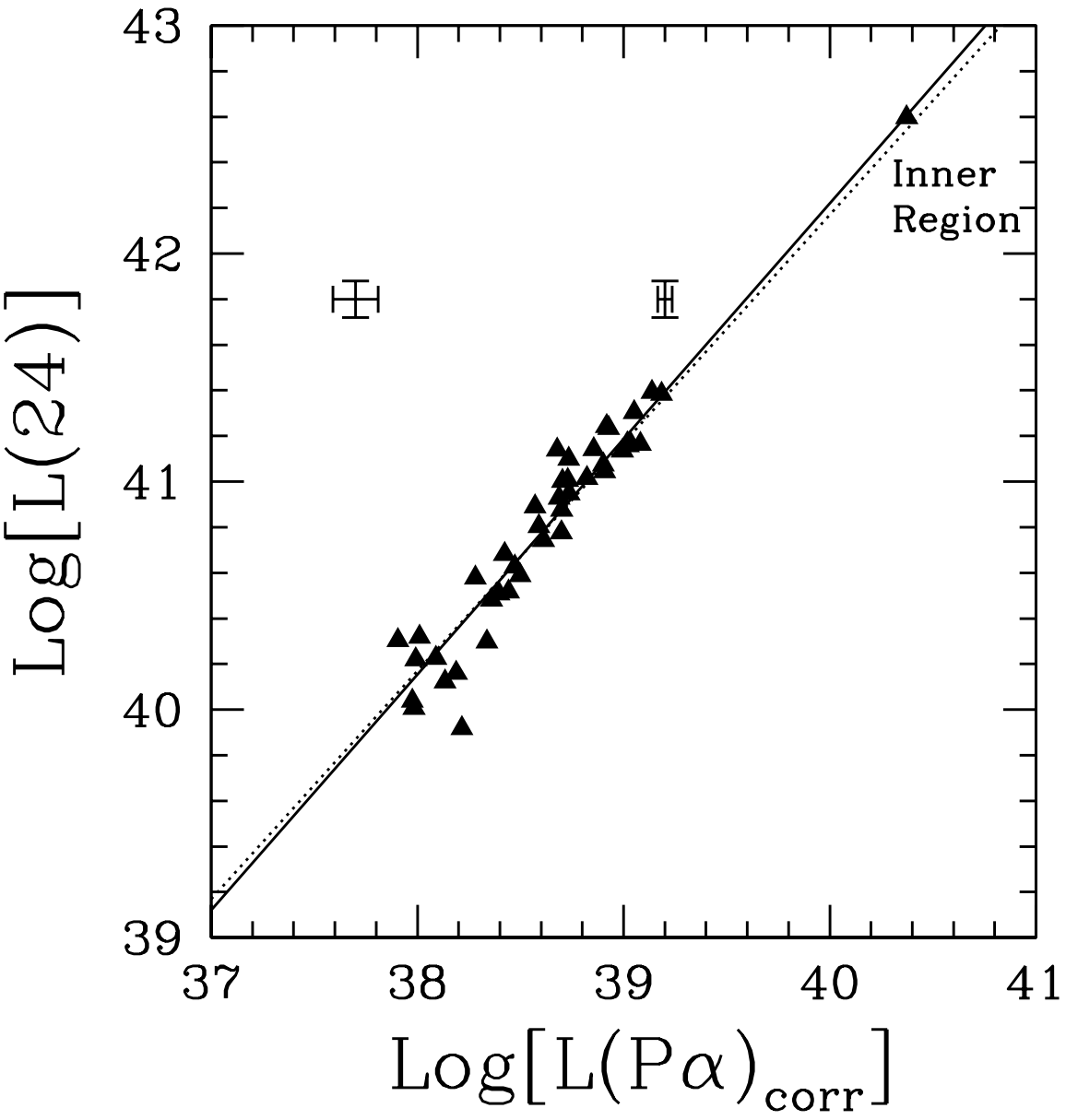

Fig. 18.— The 24 μm luminosity as a function of the extinction–corrected Pα luminosity for the 42 knots in the Inner Region. Points, lines, and error bars are as in Figure 17.

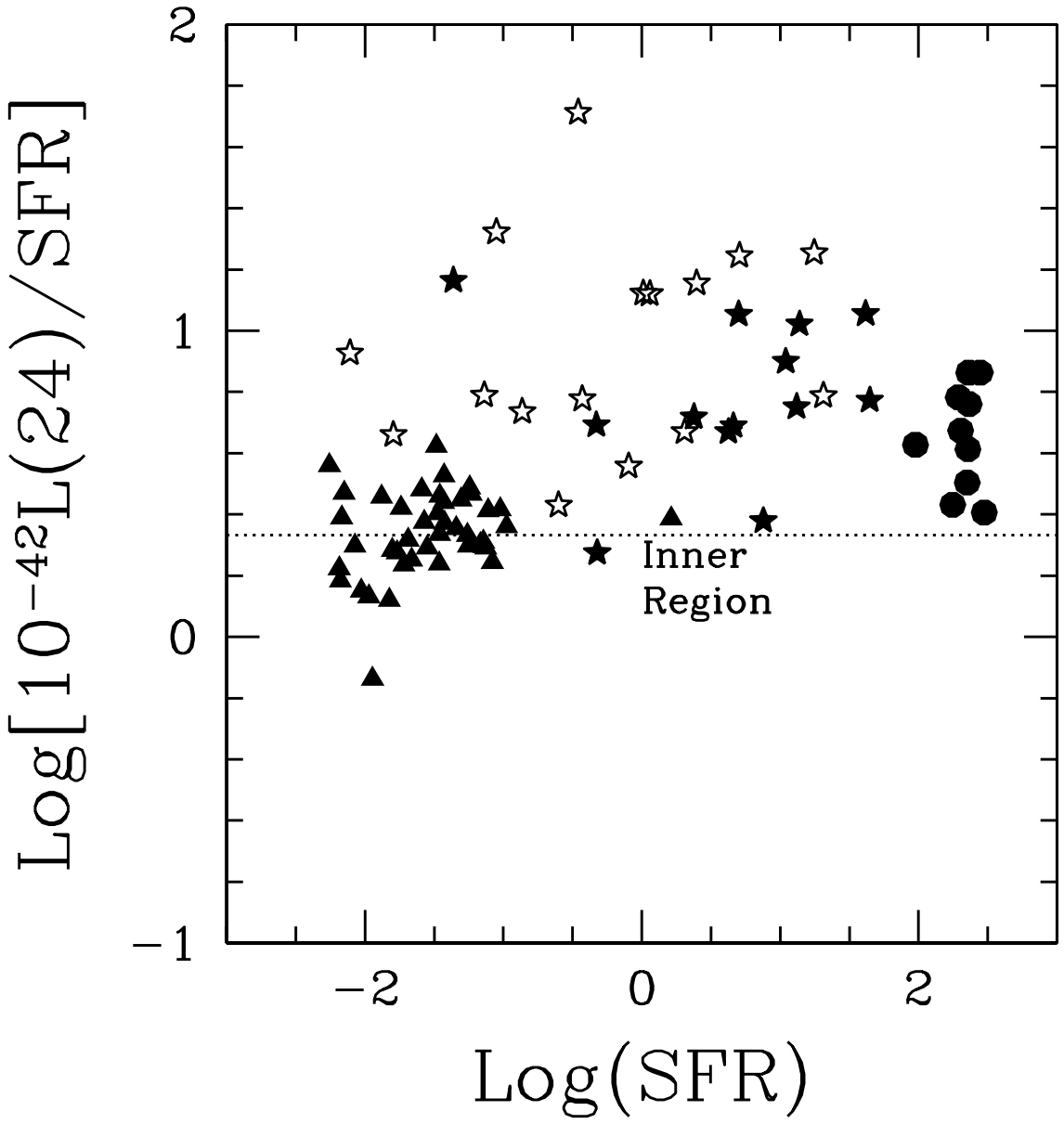

Fig. 19.— The ratio of the 24 μm luminosity to the SFR as a function of the SFR for the Inner Region's knots and for actively star–forming galaxies. The units of the horizontal and vertical axes are $M_\odot$ yr^{-1} and erg s^{-1} $(M_\odot$ yr$^{-1})^{-1}$, respectively. The SFRs for the 42 Inner Region's knots and the integrated Inner Region (filled triangles) are from the extinction–corrected Pα luminosity. The SFRs for the UV–selected starbursts are from the extinction–corrected Brγ line luminosity (filled stars; extinction correction from Hβ/Brγ Calzetti, Kinney & Storchi–Bergmann 1996) or from the extinction–corrected Hα luminosity (empty stars, extinction correction from Hα/Hβ). Starburst–dominated ULIGs (filled circles) are from Goldader et al. (2002) and Trentham, Kormendy & Sanders (1999); for these galaxies, SFRs are from the infrared luminosity using the formula of Kennicutt (1998a). For both sets of galaxies the IRAS 25 μm luminosity is used as a good approximation of MIPS24. The horizontal line is the best linear fit line through the Inner Region's knots (from Figure 18). This line is located along the lower envelope of the locus occupied by galaxies (both starbursts and

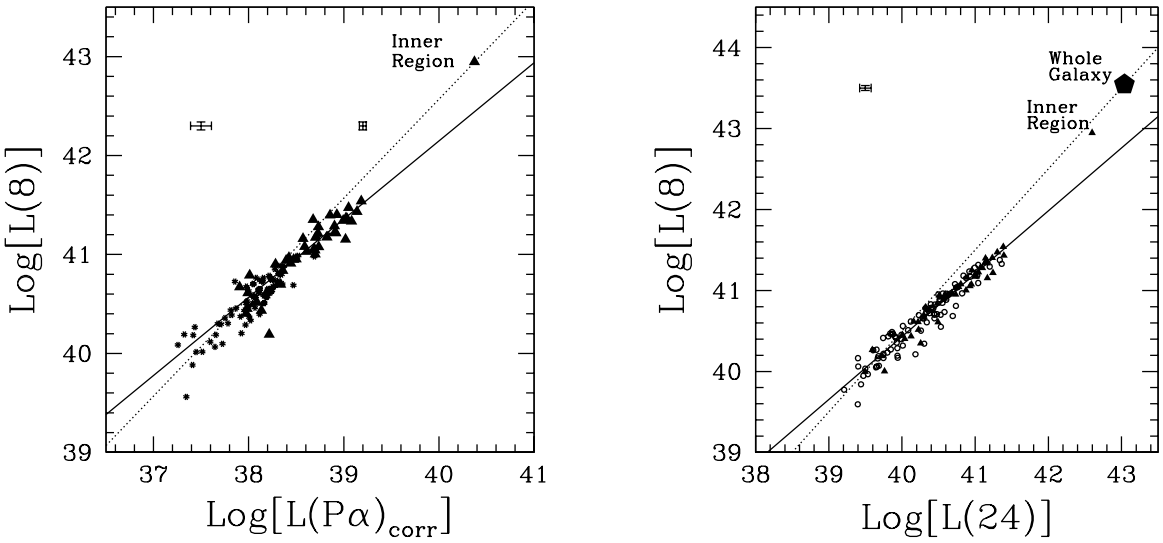

Fig. 20.— **(Left).** The 8 μm luminosity as a function of the extinction–corrected Pα luminosity in the Inner Region. Triangles indicate photometry in the 42 13″–diameter apertures, while asterisks are for the 78 4″–diameter apertures. The triangle to the right hand–side of the plot is the integrated value for the entire Inner Region. Symbols, lines, and error bars are as in Figure 17. **(Right).** The 8 μm luminosity as a function of the 24 μm luminosity in the Inner+Outer Regions. Data for the Outer Region are shown as empty circles. Integrated values for both the Inner Region and the whole galaxy (filled pentagon) are shown. The continuous line is the best fit through the Inner+Outer Regions data, while the dotted line is the slope unity relation through the whole galaxy's values.

Table 1. Positions and photometry of the HII knots.

ID[a]	RA[b] (J2000)	DEC[b] (J2000)	Log[L(FUV)][c] (erg s^{-1})	Log[L(NUV)][c] (erg s^{-1})	Log[L(U)][c] (erg s^{-1})	Log[L(B)][c] (erg s^{-1})	Log[L(Hα)][c] (erg s^{-1})	Log[L(Pα)][c] (erg s^{-1})	Log[L(8)][c] (erg s^{-1})	Log[L(24)][c] (erg s^{-1})
IR–02	13:29:53.1	47:11:55	40.91	41.16	41.41	41.73	39.10	38.92	41.34	41.16
IR–03	13:29:51.5	47:11:42	41.07	41.22	41.45	41.75	38.86	38.83	41.36	41.17
IR–04	13:29:52.6	47:11:30	41.00	41.19	41.40	41.69	38.96	38.82	41.34	41.14
IR–05	13:29:53.9	47:11:27	40.74	41.03	41.28	41.56	38.88	38.69	41.40	41.14
IR–06	13:29:54.5	47:11:40	40.86	41.12	41.33	41.60	38.94	38.84	41.37	41.16
IR–07	13:29:55.6	47:11:34	40.84	40.95	41.03	41.21	38.77	38.57	41.28	41.10
IR–08	13:29:55.7	47:11:47	41.20	41.33	41.29	41.39	39.15	38.97	41.43	41.39
IR–09	13:29:56.3	47:11:58	40.95	41.09	41.07	41.15	38.83	38.45	41.16	40.89
IR–10	13:29:54.9	47:11:58	40.60	40.94	41.07	41.29	39.03	38.76	41.29	41.07
IR–11	13:29:54.4	47:12:10	41.12	41.32	41.33	41.39	39.12	38.78	41.23	41.04
IR–12	13:29:53.2	47:12:11	40.72	40.87	40.90	41.09	38.79	38.54	41.06	40.93
IR–13	13:29:52.0	47:12:03	40.95	41.17	41.28	41.48	39.20	39.02	41.54	41.38
IR–14	13:29:50.9	47:11:57	40.65	40.87	41.12	41.33	38.98	38.87	41.47	41.30
IR–15	13:29:50.1	47:11:46	40.72	40.91	41.08	41.28	38.81	38.53	41.35	41.14
IR–16	13:29:50.1	47:11:33	40.17	40.38	40.64	40.89	38.82	38.74	41.40	41.23
IR–17	13:29:50.3	47:11:20	40.10	40.32	40.60	40.79	38.88	38.57	41.17	41.00
IR–18	13:29:51.3	47:11:29	40.70	40.91	41.13	41.40	38.72	38.56	41.21	41.01
IR–20	13:29:50.4	47:10:43	40.97	40.93	40.85	40.84	38.57	38.09	40.62	40.16
IR–21	13:29:51.6	47:10:39	40.34	40.38	40.49	40.57	38.43	37.92	40.79	40.32
IR–22	13:29:50.8	47:10:23	39.90	39.95	40.24	40.23	38.18	38.04	40.19	39.92
IR–24	13:29:53.1	47:10:40	40.96	40.97	41.03	41.11	38.64	38.27	40.94	40.51
IR–25	13:29:54.3	47:10:38	40.46	40.49	40.67	40.86	38.52	38.29	40.91	40.52
IR–28	13:30:00.6	47:11:24	40.82	40.82	40.90	41.08	38.07	37.77	40.67	40.30
IR–29	13:29:59.0	47:11:04	40.92	40.93	40.93	41.08	38.40	38.20	40.84	40.48
IR–30	13:30:00.0	47:11:12	40.75	40.76	40.83	40.97	38.87	38.66	41.17	41.02
IR–31	13:29:56.5	47:11:16	39.80	39.85	40.21	40.42	38.11	37.84	40.45	40.01
IR–32	13:29:57.3	47:11:35	40.11	40.23	40.39	40.59	38.20	37.98	40.43	40.12
IR–33	13:29:54.8	47:12:24	40.09	40.40	40.55	40.67	38.49	38.27	40.97	40.68
IR–34	13:29:56.0	47:12:27	40.42	40.60	40.75	40.84	38.78	38.36	40.95	40.63
IR–35	13:29:54.9	47:12:36	40.25	40.40	40.66	40.78	38.76	38.45	41.08	40.80
IR–36	13:29:53.3	47:12:39	40.26	40.41	40.59	40.68	39.01	38.62	41.08	40.95
IR–37	13:29:52.2	47:12:45	40.69	40.84	40.86	40.89	39.24	38.81	41.22	41.24
IR–38	13:29:50.9	47:12:44	40.32	40.45	40.54	40.59	38.79	38.55	41.00	40.87
IR–39	13:29:49.5	47:12:43	39.85	39.83	40.29	40.28	38.98	38.84	41.15	41.17

Table 1—Continued

ID[a]	RA[b] (J2000)	DEC[b] (J2000)	Log[L(FUV)][c] (erg s^{-1})	Log[L(NUV)][c] (erg s^{-1})	Log[L(U)][c] (erg s^{-1})	Log[L(B)][c] (erg s^{-1})	Log[L(Hα)][c] (erg s^{-1})	Log[L(Pα)][c] (erg s^{-1})	Log[L(8)][c] (erg s^{-1})	Log[L(24)][c] (erg s^{-1})
IR–41	13:29:47.3	47:12:22	39.68	39.70	40.05	40.01	38.60	38.35	40.95	40.59
IR–43	13:29:46.3	47:12:13	39.96	39.96	40.33	40.28	38.54	38.16	40.90	40.58
IR–47	13:29:57.6	47:11:52	40.20	40.37	40.45	40.61	38.07	37.82	40.40	40.04
IR–48	13:29:56.3	47:12:39	40.64	40.74	40.73	40.73	38.58	38.01	40.52	40.23
IR–49	13:29:47.8	47:12:36	40.53	40.59	40.69	40.78	38.57	37.93	40.61	40.22
IR–50	13:29:56.7	47:12:12	39.94	40.14	40.46	40.65	38.26	38.15	40.70	40.30
IR–53	13:29:51.9	47:11:18	40.28	40.57	40.87	41.12	38.53	38.43	41.03	40.74
IR–54	13:29:53.1	47:11:17	40.24	40.58	40.87	41.16	38.51	38.50	41.04	40.78
01–01	13:29:52.8	47:13:54	40.42	40.42	40.37	40.57	38.61	...	40.66	40.28
01–02	13:29:53.7	47:13:37	39.95	40.05	39.88	40.03	38.27	...	40.49	39.86
01–04	13:29:50.5	47:13:56	40.00	40.00	40.05	40.06	38.70	...	40.72	40.38
01–05	13:29:49.6	47:13:28	39.91	39.95	39.77	39.91	38.25	...	40.70	40.45
01–06	13:29:47.5	47:13:25	40.31	40.29	39.99	40.08	38.41	...	40.78	40.32
01–07	13:29:47.2	47:13:39	41.14	41.10	40.90	41.05	38.91	...	40.72	40.44
01–08	13:29:46.0	47:13:45	40.70	40.63	40.41	40.45	38.68	...	40.29	39.94
01–09	13:29:45.1	47:13:32	40.58	40.59	40.46	40.55	38.87	...	40.95	40.50
01–12	13:29:50.8	47:13:22	40.28	40.31	40.22	40.44	37.88	...	40.07	39.69
02–02	13:29:38.9	47:12:13	40.22	40.09	39.96	40.08	38.06	...	40.16	39.67
02–03	13:29:38.3	47:12:03	39.96	39.96	39.83	39.93	37.98	...	40.17	39.75
02–08	13:29:40.7	47:11:35	40.29	40.33	40.18	40.43	38.03	...	40.43	39.91
02–09	13:29:38.7	47:11:05	40.45	40.44	40.31	40.54	31.65	...	39.84	39.44
03–01	13:29:37.1	47:09:46	40.25	40.24	40.24	40.44	38.72	...	40.73	40.33
03–03	13:29:39.4	47:08:40	40.35	40.24	40.32	40.43	39.09	...	41.04	40.74
03–12	13:29:38.6	47:08:57	39.16	39.39	38.98	39.42	38.07	...	40.41	39.92
03–14	13:29:40.2	47:08:25	38.13	39.23	38.89	39.07	38.12	...	40.45	39.99
04–01	13:29:46.4	47:12:33	40.65	40.72	40.59	40.81	38.75	...	40.73	40.58
04–03	13:29:43.1	47:11:38	41.15	41.20	41.01	41.21	38.71	...	40.78	40.43
04–04	13:29:42.0	47:11:11	40.43	40.47	40.36	40.54	38.70	...	40.89	40.52
04–05	13:29:42.8	47:10:49	40.53	40.57	40.47	40.74	38.52	...	40.65	40.29
04–06	13:29:42.8	47:11:02	40.20	40.29	40.32	40.69	38.30	...	40.66	40.44
04–07	13:29:43.3	47:11:21	40.24	40.35	40.29	40.63	37.99	...	40.70	40.23
04–08	13:29:45.4	47:10:51	40.21	40.41	40.94	41.39	37.94	...	40.40	39.99
04–09	13:29:45.0	47:12:26	40.55	40.55	40.39	40.64	38.26	...	40.36	39.93
05–01	13:29:44.2	47:10:23	41.18	41.18	41.01	41.17	39.47	...	41.38	41.34

Table 1—Continued

ID[a]	RA[b] (J2000)	DEC[b] (J2000)	Log[L(FUV)][c] (erg s^{-1})	Log[L(NUV)][c] (erg s^{-1})	Log[L(U)][c] (erg s^{-1})	Log[L(B)][c] (erg s^{-1})	Log[L(Hα)][c] (erg s^{-1})	Log[L(Pα)][c] (erg s^{-1})	Log[L(8)][c] (erg s^{-1})	Log[L(24)][c] (erg s^{-1})
05–02	13:29:44.8	47:09:58	41.37	41.33	41.12	41.25	39.37	...	41.30	41.20
05–03	13:29:43.5	47:10:00	40.33	40.48	40.40	40.61	38.75	...	40.97	40.67
05–04	13:29:46.9	47:09:39	41.05	41.02	40.84	41.01	38.76	...	40.71	40.48
05–06	13:29:47.9	47:10:29	40.40	40.44	40.30	40.58	38.21	...	40.32	40.01
05–07	13:29:50.7	47:10:22	40.01	40.13	39.97	40.33	38.15	...	40.19	39.94
05–08	13:29:50.4	47:09:44	40.64	40.66	40.55	40.71	38.81	...	40.96	40.56
05–09	13:29:49.0	47:09:19	40.21	40.16	40.14	40.38	38.13	...	40.47	39.84
05–10	13:29:50.6	47:09:21	40.65	40.67	40.52	40.69	38.57	...	40.77	40.34
05–11	13:29:51.9	47:09:22	39.70	39.91	39.34	39.79	38.01	...	40.23	39.80
05–13	13:29:44.2	47:09:36	40.38	40.27	40.01	40.24	38.19	...	40.41	39.74
05–14	13:29:45.1	47:09:26	40.10	40.00	39.63	39.82	38.21	...	40.16	39.40
05–17	13:29:53.5	47:10:15	40.79	40.77	40.52	40.74	37.91	...	40.05	39.65
05–19	13:29:54.6	47:10:18	40.72	40.76	40.56	40.79	38.08	...	40.06	39.66
06–07	13:29:49.2	47:08:09	39.98	40.06	39.88	40.07	37.74	...	39.59	39.40
06–09	13:29:53.5	47:08:37	40.32	40.21	39.98	40.18	38.10	...	40.19	39.68
06–10	13:29:51.9	47:08:24	39.86	39.89	39.44	39.45	37.99	...	39.97	39.53
06–11	13:29:52.8	47:08:46	40.56	40.50	40.26	40.47	38.28	...	40.22	39.75
07–01	13:30:01.4	47:12:50	41.01	40.99	40.79	40.96	39.09	...	41.33	41.36
07–02	13:30:00.7	47:13:07	41.13	41.10	40.93	41.09	39.22	...	41.32	41.04
07–03	13:30:00.4	47:13:18	41.05	41.02	40.85	41.03	39.01	...	41.24	40.92
07–04	13:29:59.9	47:13:31	41.08	41.00	40.83	41.03	38.98	...	41.18	40.84
07–05	13:29:59.6	47:13:58	41.14	41.13	40.95	41.02	39.34	...	41.17	40.94
07–06	13:29:58.7	47:14:08	40.88	40.90	40.74	40.79	39.03	...	40.97	40.82
07–07	13:29:57.6	47:13:56	40.75	40.76	40.65	40.81	38.78	...	40.98	40.70
07–08	13:29:58.6	47:13:49	40.91	40.92	40.80	40.96	39.03	...	41.04	40.75
07–09	13:29:59.9	47:13:43	41.06	41.01	40.81	40.97	38.81	...	40.96	40.61
07–10	13:30:04.7	47:13:03	40.98	40.91	40.70	40.80	38.70	...	40.79	40.40
07–12	13:29:55.5	47:14:01	40.74	40.71	40.56	40.63	39.00	...	41.15	40.88
07–13	13:29:55.7	47:13:48	40.29	40.30	40.28	40.45	38.70	...	40.93	40.61
07–14	13:29:53.9	47:14:05	40.19	40.12	40.08	40.15	38.30	...	40.61	40.34
07–15	13:30:02.0	47:13:01	41.37	41.31	41.09	41.27	38.64	...	40.69	40.69
07–16	13:30:01.1	47:13:32	41.32	41.29	40.99	41.15	38.45	...	40.21	40.18
07–17	13:30:01.3	47:13:45	41.18	41.15	40.92	41.04	38.23	...	40.17	39.94
07–18	13:30:03.0	47:12:46	40.84	40.84	40.62	40.77	38.57	...	40.83	40.45

Table 1—Continued

ID[a]	RA[b] (J2000)	DEC[b] (J2000)	Log[L(FUV)][c] (erg s^{-1})	Log[L(NUV)][c] (erg s^{-1})	Log[L(U)][c] (erg s^{-1})	Log[L(B)][c] (erg s^{-1})	Log[L(Hα)][c] (erg s^{-1})	Log[L(Pα)][c] (erg s^{-1})	Log[L(8)][c] (erg s^{-1})	Log[L(24)][c] (erg s^{-1})
08–01	13:29:56.5	47:10:45	40.41	40.47	40.53	40.75	38.88	...	41.28	41.00
08–02	13:29:60.0	47:11:12	40.74	40.78	40.68	40.90	38.88	...	41.19	41.03
08–03	13:30:00.9	47:11:37	40.96	40.97	40.83	41.04	38.90	...	41.08	40.73
08–04	13:30:01.7	47:11:47	40.60	40.66	40.61	40.86	38.60	...	40.95	40.64
08–05	13:30:02.0	47:11:59	40.61	40.60	40.49	40.70	38.67	...	40.92	40.59
08–06	13:30:03.3	47:12:19	40.54	40.51	40.20	39.97	38.85	...	40.90	40.57
08–07	13:30:01.6	47:12:14	40.07	40.21	40.26	40.58	38.08	...	40.75	40.37
08–08	13:30:03.7	47:12:35	40.48	40.41	39.78	40.14	38.51	...	40.83	40.39
08–09	13:29:57.6	47:10:45	40.90	40.94	40.84	41.10	38.44	...	40.85	40.55
08–10	13:29:59.0	47:11:03	40.93	40.96	40.82	41.06	38.43	...	40.89	40.61
08–11	13:30:05.0	47:12:32	41.08	41.03	40.76	40.88	38.05	...	40.42	39.91
09–01	13:29:55.7	47:09:13	40.11	40.15	39.99	40.10	38.05	...	40.46	39.87
09–03	13:29:58.8	47:09:13	40.95	40.89	40.68	40.77	38.84	...	40.76	40.40
09–04	13:30:00.9	47:09:28	40.43	40.43	40.38	40.24	38.87	...	40.50	40.26
09–05	13:30:02.4	47:09:46	40.88	40.83	40.73	40.82	39.29	...	41.09	41.04
09–06	13:30:03.0	47:09:57	40.78	40.78	40.59	40.70	38.99	...	40.81	40.74
09–07	13:30:03.4	47:09:40	40.67	40.63	40.48	40.59	38.86	...	40.70	40.53
09–08	13:30:04.3	47:10:03	40.58	40.51	40.35	40.51	38.28	...	40.47	39.88
09–09	13:30:04.9	47:10:22	40.64	40.57	40.34	40.44	38.37	...	40.56	40.01
09–10	13:30:04.8	47:10:35	39.95	39.92	39.81	39.77	38.41	...	40.62	40.12
09–11	13:30:03.8	47:10:15	40.68	40.63	40.42	40.57	37.86	...	39.95	39.47
09–12	13:29:54.6	47:09:04	40.66	40.59	40.40	40.56	38.17	...	40.26	39.61
10–01	13:30:07.0	47:11:35	40.80	40.73	40.56	40.67	38.74	...	40.51	40.08
10–02	13:30:08.1	47:11:38	40.01	40.06	39.60	39.76	38.30	...	40.03	39.50
10–03	13:30:06.7	47:11:22	40.55	40.49	40.25	40.28	38.44	...	39.77	39.21
10–05	13:30:07.0	47:12:27	40.47	40.43	40.19	40.26	38.52	...	40.43	39.81
10–06	13:30:07.7	47:12:43	40.23	40.21	40.06	40.15	38.44	...	40.27	39.85
10–11	13:30:06.8	47:14:19	40.83	40.71	40.48	40.47	38.44	...	40.06	39.40
11–02	13:30:04.0	47:15:34	40.49	40.41	40.25	40.34	38.74	...	40.55	40.53
11–03	13:30:03.6	47:15:46	40.40	40.32	40.25	40.37	38.66	...	40.34	40.30

[a]Identification of the HII knots for which photometry has been measured in 13″ diameter apertures. The ID format XX–YY identifies the background region (XX) where the aperture is located and an internal progressive number (YY) for the aperture.

[b]Position on the sky of the aperture.

[c]ogarithm of the luminosities in the FUV and NUV from GALEX, U, B, and Hα(λ0.6563 μm) from ground–based images, Pα(λ1.8756 μm) from HST/NICMOS, and 8 μm and 24 μm from Spitzer/IRAC and MIPS. Stellar continuum luminosities are given as λL(λ). The central wavelengths of the U and B filters are 0.4312 μm and 0.3463 μm, respectively. Stellar and ionized gas luminosities have been corrected for the Galactic foreground extinction E(B$-$V)$_{MW}$=0.037.

This figure "f1a.jpg" is available in "jpg" format from:

http://arXiv.org/ps/astro-ph/0507427v1

This figure "f1b.jpg" is available in "jpg" format from:

http://arXiv.org/ps/astro-ph/0507427v1

This figure "f2.jpg" is available in "jpg" format from:

http://arXiv.org/ps/astro-ph/0507427v1

This figure "f3a.jpg" is available in "jpg" format from:

http://arXiv.org/ps/astro-ph/0507427v1

This figure "f3b.jpg" is available in "jpg" format from:
http://arXiv.org/ps/astro-ph/0507427v1

This figure "f3c.jpg" is available in "jpg" format from:

http://arXiv.org/ps/astro-ph/0507427v1

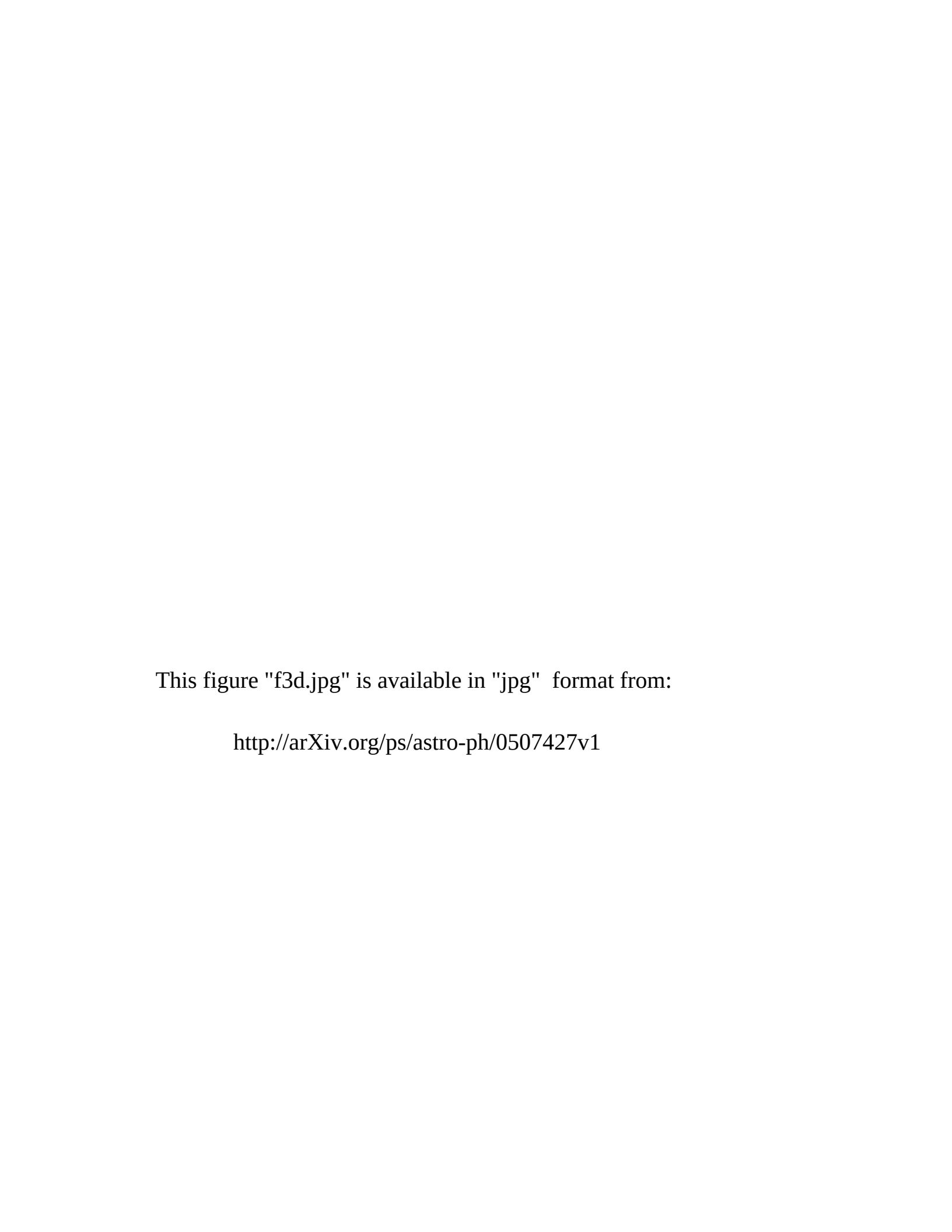
This figure "f3d.jpg" is available in "jpg" format from:
http://arXiv.org/ps/astro-ph/0507427v1

This figure "f4a.jpg" is available in "jpg" format from:

http://arXiv.org/ps/astro-ph/0507427v1

This figure "f4b.jpg" is available in "jpg" format from:
http://arXiv.org/ps/astro-ph/0507427v1